

1 **Influence of street trees on turbulent fluctuations**
2 **and transport processes in an urban canyon: a wind**
3 **tunnel study**

4 **Annika Vittoria Del Ponte**^{1,2} · **Sofia**
5 **Fellini**^{1,2} · **Massimo Marro**² · **Maarten**
6 **van Reeuwijk**³ · **Luca Ridolfi**¹ · **Pietro**
7 **Salizzoni**^{1,2}

8
9 the date of receipt and acceptance should be inserted later

10 **Abstract**

11 The presence of vegetation within urban canyons leads to non-trivial pat-
12 terns of the concentration of airborne pollutants, as a result of the complex
13 structure of the velocity field. To investigate the relationship between concen-
14 tration, velocity fields and vegetation density, we have performed wind-tunnel
15 experiments in a reduced-scale street canyon, oriented perpendicular to the
16 external wind flow, within which we placed a steady ground-level line source
17 of a passive tracer. The aerodynamic behavior of vegetation was reproduced
18 by inserting plastic miniatures of trees along the two long sides of the canyon,
19 according to three different densities. The canyon ventilation was investigated
20 by acquiring one-point simultaneous statistics of concentration and velocity
21 over a dense grid of points within the canyon. The results show that the pres-
22 ence of trees hinders the upward mean vertical velocity at the rooftop, causes
23 a reduction of the turbulent kinetic energy inside the canyon, and reduces the
24 energy content of the large scales. The scalar concentration is conversely char-
25 acterized by an enhanced level of turbulent fluctuations, whose magnitude is
26 not dampened increasing the tree density. Within the canyon, high tree den-
27 sity inhibits turbulent mass fluxes, which are instead enhanced at roof level,
28 where the mean component of the scalar flux is however hindered. A statistical
29 analysis of concentration time series reveals that the lognormal distribution is

¹ Department of Environmental, Land, and Infrastructure Engineering, Politecnico di Torino
Corso Duca degli Abruzzi 24, 10129 Turin, Italy
Tel.: +39 011 090 7602
Fax: +39 011 090 7699
E-mail: annika.delponte@polito.it

² Univ Lyon, Ecole Centrale de Lyon, CNRS, Univ Claude Bernard Lyon 1, INSA Lyon,
LMFA
UMR5509, 69130, Ecully France

³Imperial College London, Department of Civil and Environmental Engineering
SW7 2AZ, London, United Kingdom

30 suitable to model concentration fluctuations and extreme events, in dispersing
31 plumes emitted by a linear source.

32 **Keywords** Mass transport · Street canyon · Trees · Ventilation · Wind-tunnel
33 experiments

34

35 1 Introduction

36 Inserting vegetation in the urban environment is a promising strategy to mit-
37 igate the urban heat island effect and to reduce flood risks and air pollution
38 levels (Ferrini et al. 2020). The presence of trees in cities guarantees shading
39 and evapotranspiration, which are fundamental for temperature regulation
40 (Oliveira et al. 2011; Grilo et al. 2020). Green areas increase the amount of
41 permeable surface and therefore the infiltration capacity of urban terrain. This
42 ensures the regulation of stormwater runoff, and an increase of soil moisture
43 for evapotranspiration (Armson et al. 2013; Zölch et al. 2017). Thanks to the
44 large surface area of the leaves, tree crowns act as sinks of pollutants as they
45 promote dry deposition and absorption (Hewitt et al. 2020; Diener and Mudu
46 2021). Moreover, during the daytime, photosynthesis guarantees CO₂ seques-
47 tration (Nowak and Crane 2002; Ferrini and Fini 2011). Besides, green areas
48 offer human and ecosystem well-being, providing natural areas for amusement,
49 increasing biodiversity, and attenuating noise pollution (Van Renterghem et al.
50 2015).

51 However, urban vegetation may also have adverse effects on street venti-
52 lation and air quality. Notably, vegetation alters pollutant dispersion mecha-
53 nisms, depending on its density, its spatial configuration, as well as the relative
54 location of the pollutant source (Abhijith et al. 2017). Recently, Grylls and van
55 Reeuwijk (2022) employed Large Eddy Simulations (LES) to study the effects
56 of trees on air quality in street canyons, using a vegetation model that incor-
57 porates deposition, shading, and aerodynamic drag (Grylls and van Reeuwijk
58 2021) and analysing the two competing processes affecting air quality: the
59 beneficial role of deposition on the leaves and the reduced ventilation induced
60 by trees aerodynamics.

61 Experimentally, the aerodynamic effect of vegetation on pollutant disper-
62 sion in urban areas was studied in wind tunnels, as recently reviewed by Zhao
63 et al. (2023), laying reduced-scale vegetation in model street canyons. Gromke
64 and Ruck (2007) performed concentration measurements in an isolated street
65 canyon, oriented perpendicular to the wind flow, with a row of model trees
66 placed along the central axis. They found that the presence of trees causes an
67 increase of the mean pollutant concentration close to the upwind building and
68 a decrease in it close to the downwind building. These effects are more pro-
69 nounced with greater tree crown diameter or smaller tree spacing, whereas the
70 crown porosity causes remarkable concentration variations only if it is greater
71 than 97% (Gromke and Ruck 2009). With a wind blowing with an angle of
72 45° with respect to the canyon axis, the increase of pollutant concentration

73 due to the presence of trees is still detectable, but not when the wind flow is
74 parallel to the canyon axis (Gromke and Ruck 2012). A vegetation-induced in-
75 crease of the mean concentration within urban canyons was also observed with
76 Reynolds-averaged Navier–Stokes simulations (Gromke et al. 2008; Buccolieri
77 et al. 2009) and LES (Moonen et al. 2013; Merlier et al. 2018). In a recent
78 work, Fellini et al. (2022) presented the results of an experimental campaign
79 aimed at providing a high-resolution three-dimensional characterization of the
80 mean scalar concentration field inside a vegetated street canyon, perpendicu-
81 lar to the wind flow. They found that different spatial patterns of the mean
82 concentration emerge depending on the tree density. Moreover, the presence of
83 trees increases the pollutant concentration at the upwind wall, mostly at the
84 pedestrian level, even if it does not affect significantly the average concentra-
85 tion calculated over the whole canyon. All papers cited above focused on the
86 spatial distribution of the time-averaged concentration within street canyons.
87 In the present work, we aim at extending this investigation to the estimation
88 of the turbulent mass fluxes, within the canyon, which drive the transfer of
89 pollutant towards the external atmosphere.

90 The issue of the turbulent (mass and momentum) transfer between the
91 external flow and a plant (Raupach et al. 1996; Finnigan 2000) or urban (Gar-
92 bero et al. 2010; Neophytou et al. 2014; Perret et al. 2019) canopy has been
93 so far addressed by a large number of authors. On one side, studies on plant
94 canopies were conducted adopting idealised (Raupach et al. 1986; Poggi et al.
95 2006) or (more rarely) realistic (Pietri et al. 2009) modeled trees, focusing
96 on the role of vegetation density (Poggi et al. 2004) and terrain morphology
97 (Poggi and Katul 2007a,b). On the other side, most studies on the urban
98 canopy considered simplified urban geometries, focusing on the effect of the
99 canyon height-to-width ratio (H/W_c , where H is the height of the canyon and
100 W_c is its width) (Di Bernardino et al. 2015, 2018; Jaroslowski et al. 2020),
101 upstream turbulence (Salizzoni et al. 2011; Blackman et al. 2015, 2018) and
102 thermal fluxes (Marucci and Carpentieri 2019; Fellini et al. 2020) on the street
103 canyon ventilation.

104 Studies focusing on the combined effect of both trees and building density
105 on turbulence dynamics are however still missing. This study is a first step,
106 forward to fill this gap. After describing the wind tunnel facility (section 2)
107 and the measurement techniques (section 3), in section 4, we present flow
108 (subsection 4.1) and concentration fields (subsection 4.2) and of the vertical
109 mass fluxes (subsection 4.3), within and above the street canyon. In section
110 4.2.1 we provide a probabilistic characterization of concentration fluctuations,
111 with a focus on extreme values, which have important applications in toxic
112 risk analysis. Conclusions are drawn in section 5.

113 2 Experimental setup

114 The experimental campaign was carried out in the atmospheric wind tunnel
115 of the Laboratoire de Mécanique des Fluides et d’Acoustique (LMFA), at

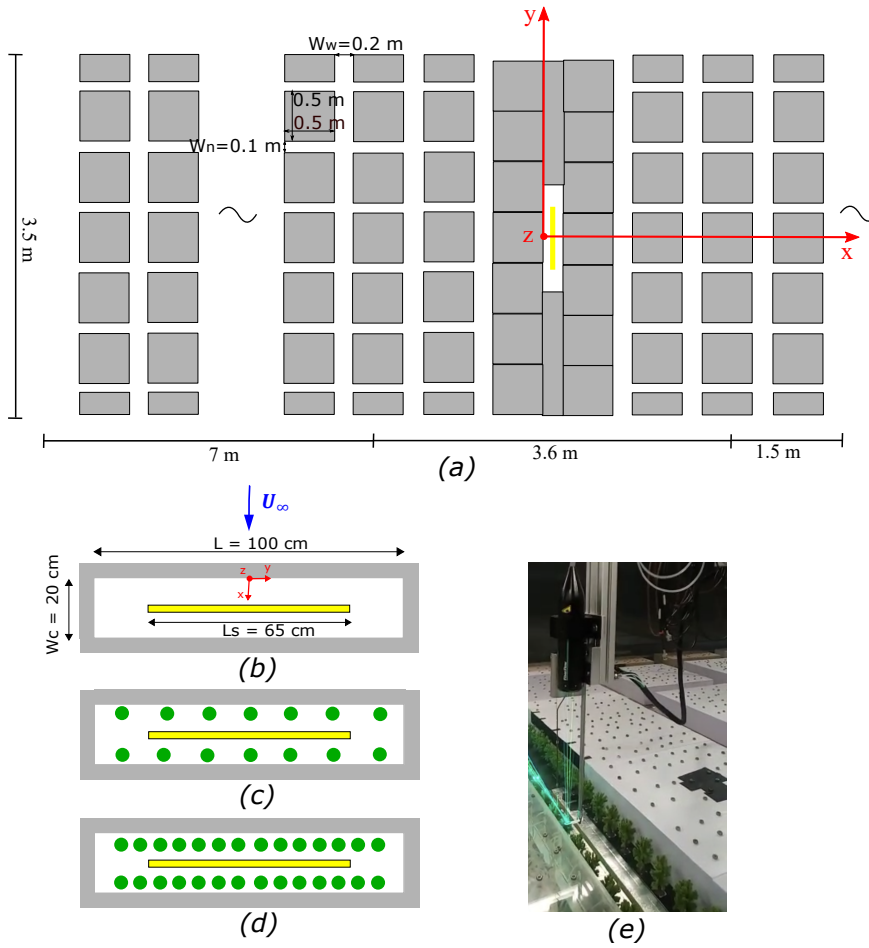


Fig. 1 (a) Scheme of the urban network reproduced inside the test section of the wind tunnel. (b) Reference street canyon in the Zero (b), Half (c), and Full (d) configurations. The yellow line represents the linear source, while the green dots are the model trees. (e) System LDA-FID coupled with the mirror.

116 the École Centrale de Lyon. It is a recirculating system, with a test section
 117 12 m long, 2 m high and 3.5 m wide. Inside the test section, an urban street
 118 network in scale 1:200, with a geometry similar to the one adopted by Garbero
 119 et al. (2010), was created using model buildings 0.1 m high, spaced by 0.2
 120 m in the streamwise direction and by 0.1 m in the spanwise direction (Fig.
 121 1a). Narrower streamwise streets ($H/W_n=1$) and wider perpendicular streets
 122 ($H/W_w=0.5$) were arranged to avoid flow channeling. The roughness of the
 123 roofs was reproduced with 5 mm high steel nuts, randomly placed on the
 124 top of the blocks. A wind flow was generated by an axial fan, installed in
 125 the upper conduit of the recirculating wind tunnel. The turbulent flow was
 126 developed placing a homogeneous turbulent grid and a row of 7 Irwin spires,

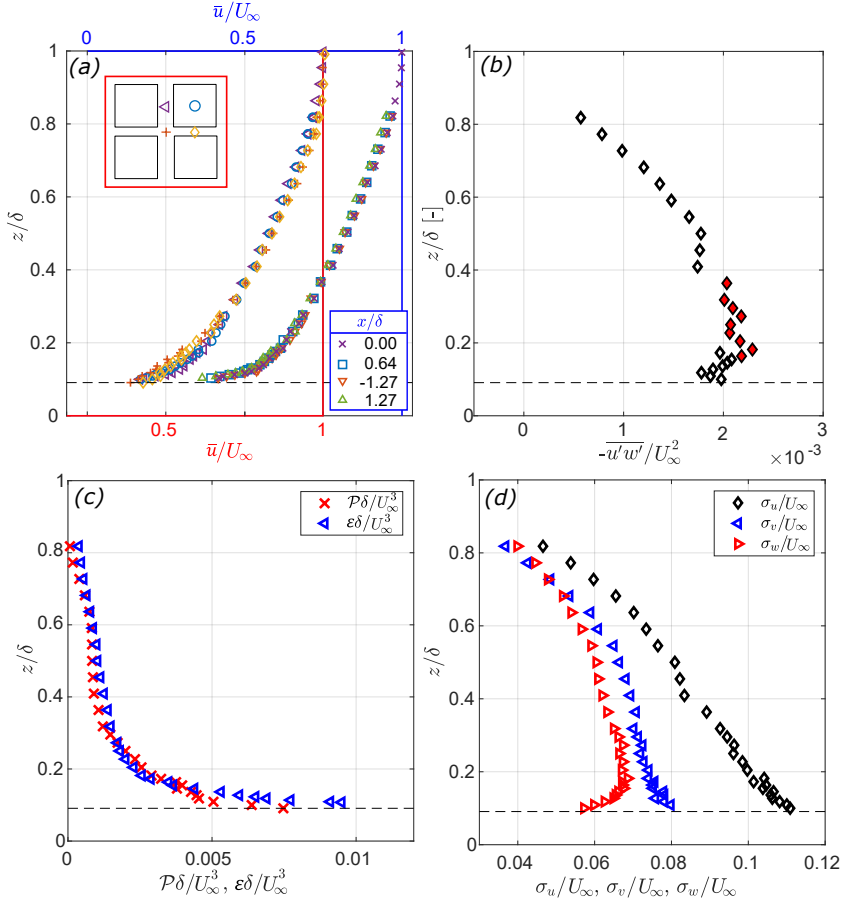


Fig. 2 (a) Streamwise mean velocity profiles at the top of the building-like obstacles (black dashed line), measured at 4 different positions around a building-like-obstacle (red bottom x -axis) and at 4 different distances along the streamwise direction of the wind tunnel (blue top x -axis). (b) Reynolds stresses. The full markers represent the constant-stress region. (c) Production and dissipation rate of turbulent kinetic energy. (d) Standard deviation of the three velocity components.

127 0.95 m high, at the entrance of the test section. The interaction of the wind
 128 flow with the grid, the spires and the rough blocks on the floor generates
 129 a neutrally stratified boundary layer of depth $\delta=1.1\text{m}$, with a free-stream
 130 velocity $U_\infty = \bar{u}(z = \delta)=5\text{m/s}$, where \bar{u} is the mean streamwise velocity. The
 131 Reynolds number of the flow is $Re = \delta U_\infty / \nu \simeq 3.6 \times 10^5$, where $\nu \simeq 1.52 \times 10^{-5}$
 132 m^2/s is the kinematic viscosity of the air at 19°C , which guarantees Reynolds
 133 independent flow dynamics (Allegrini et al. 2013; Marucci and Carpentieri
 134 2019). In the lower part of this boundary layer, in the so-called inertial layer,
 135 the mean velocity profile is well fitted by a logarithmic profile of the form

$$\bar{u}(z) = \frac{u_*}{\kappa} \ln\left(\frac{z-d}{z_0}\right), \quad (1)$$

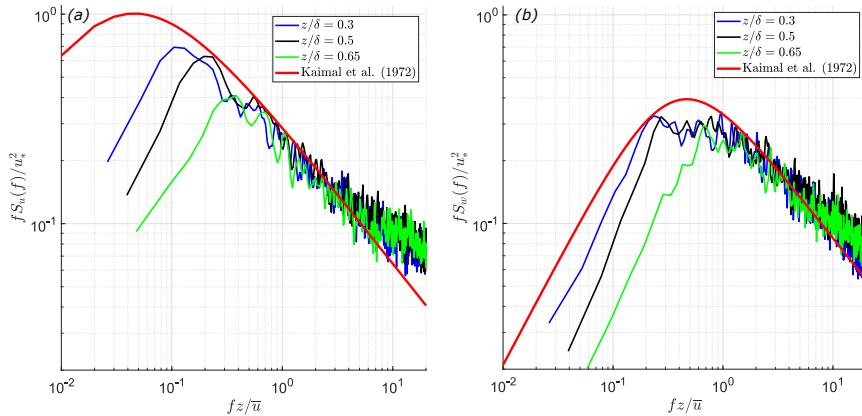


Fig. 3 Velocity spectra of the streamwise velocity (a) and of the vertical velocity (b) for growing distances from the obstacles, z/δ . The empirical spectra $S_u(f)$ and $S_w(f)$ are compared with a model extrapolated from field data (Kaimal et al. 1972), represented with the red line.

136 where $u_*=0.29$ m/s is the friction velocity, $\kappa=0.4$ is the von Kármán constant,
 137 $d=0.094$ m is the zero-plane displacement, and $z_0 = 1 \times 10^{-3}$ m is
 138 the aerodynamic roughness length. We defined the inertial region isolating
 139 the fraction of the mean velocity profile that lays on a straight line in the
 140 semi-logarithmic plot. To obtain a precise delimitation of the inertial zone, we
 141 explored different extensions of the linear region above the roughness sub-layer
 142 in the range $0.15 < z/\delta < 0.4$ (Fellini et al. 2022). We selected u_* , d and z_0
 143 so as to minimize the sum of the square difference between the logarithmic
 144 law (equation 1) and the velocity measurements in the linear region (Salizzoni
 145 et al. 2008). Furthermore, we verified that u_* is consistent with the value of
 146 Reynolds stresses according to the relation $u_*^2 = -\overline{u'w'}$ (Fig. 2b). In Fig. 2a,
 147 we report vertical profiles of \bar{u} measured at four different positions around a
 148 building-like-obstacles – above the rooftop, above a streamwise street, above a
 149 spanwise street, and above a street intersection – and at different streamwise
 150 distances from the entrance of the test section. The vertical profiles collapse
 151 onto a single curve, meaning that the external boundary layer has reached an
 152 equilibrium condition. Consistently, the Reynolds stress profile clearly exhibits
 153 a constant stress region in the lower part of the velocity field (Fig. 2b) and pro-
 154 duction (\mathcal{P}) and dissipation (ε) of turbulent kinetic energy overlap throughout
 155 the whole boundary layer (Fig. 2c). The profiles of the standard deviation of
 156 the streamwise, transversal, and vertical velocity components (defined in Fig.
 157 2d as σ_u , σ_v , and σ_w , respectively) show typical shapes of a neutral boundary
 158 layer (Raupach et al. 1991; Salizzoni et al. 2008; Garbero et al. 2010). Finally,
 159 we report the spectra of the streamwise velocity signal ($u(t)$) and of the verti-
 160 cal velocity signal ($w(t)$) for increasing distances from the obstacles (see Fig.
 161 3). We compare them to the model proposed by Kaimal et al. (1972), based

162 on the Kansas field experiments:

$$\frac{fS_u(f)}{u_*^2} = \frac{105n}{(1 + 33n)^{5/3}} \quad (2)$$

163

$$\frac{fS_w(f)}{u_*^2} = \frac{2n}{1 + 5.3n^{5/3}} \quad (3)$$

164 where f is the constant sampling frequency, $S_u(f)$ and $S_w(f)$ are the spectra
 165 of $u(t)$ and $w(t)$, respectively, $n = fz/\bar{u}$ in the non-dimensional frequency,
 166 z is the vertical distance, and \bar{u} is the local mean longitudinal velocity. The
 167 measured spectra show a good agreement with the Kaimal's model in the
 168 inertial region, meaning that the empirical spectra are similar to atmospheric
 169 spectra. Further details on the experimental facility and on the evaluation of
 170 the boundary layer parameters, ε , and \mathcal{P} are available in Fellini et al. (2022).

171 The reference street canyon is a closed cavity $L=1\text{m}$ long, $H=0.1\text{m}$ high,
 172 $W_c=0.2\text{m}$ wide, within which the scalar ground-level line source is placed. We
 173 adopted a canyon with lateral edges bordered by walls in order to avoid lateral
 174 mass fluxes and to define a control volume for the rigorous estimation of the
 175 ventilation efficiency, performing a mass balance between the mass flux emitted
 176 by the line source and the mass flux leaving the canyon at the rooftop.
 177 The geometry of the street canyon provides an aspect ratio $H/W_c=0.5$ and
 178 a length to height ratio $L/H=10$, which approximates the characteristics of
 179 an indefinitely long canyon (Salizzoni et al. 2009; Allegrini et al. 2013). The
 180 canyon is around 9 m away from the entrance of the test section, and it is oriented
 181 perpendicular to the wind flow direction. The ground-level linear source
 182 (simulating traffic pollutant emissions) is $L_s=0.65$ m long, thus it does not
 183 cover the entire length of the canyon (see yellow line in Fig. 1b), in order to
 184 avoid wall effects. It consists of a metallic tube pierced with needles emitting
 185 an ethane-air mixture within a homogenization chamber, located in a slot cut
 186 in the floor of the wind tunnel. From this chamber, the gas mixture is injected
 187 in the canyon, at ground level, through a metallic grid 65cm long and
 188 1cm wide. The small holes of the grid produce substantial pressure drop thus
 189 rendering the gas flow in the street canyon insensitive to local pressure fluctuations.
 190 The injection flow rate is 0.4 l/min, allowing an emission velocity
 191 (equal to 0.01 m/s) sufficiently low to avoid flow perturbation in the cavity
 192 (Marro et al. 2020). Ethane was chosen as a passive tracer since it has a density
 193 similar to air. The origin of the reference system was assumed in the middle
 194 of the street canyon, at the upwind wall (see red arrows in Fig. 1a,b), with the
 195 x -coordinate oriented in the streamwise direction, the y -coordinate oriented
 196 along the canyon axis and the z -coordinate oriented upward.

197 The urban vegetation was simulated through plastic miniatures of trees,
 198 with a trunk of 2 cm and a porous crown, made of plastic filaments, 6.5
 199 cm high and 4.5 cm wide. In a 1:200 scale, the miniatures represent trees
 200 16m high and 9m wide, similar to plane trees or hypochestnuts, typically
 201 planted in tree-lined boulevards located in urban canyons flanked by buildings
 202 20m high. The aerodynamic behavior of the model trees was characterized

203 measuring their aerodynamic porosity and drag coefficient (Fellini et al. 2022).
 204 The aerodynamic porosity is the ratio between the spatial average wind speed
 205 downstream the obstacle and the average speed of the approaching wind. It
 206 was evaluated performing velocity measurements on a dense grid upstream and
 207 downstream a single tree, placed in a homogeneous flow. The velocity field was
 208 integrated over the tree silhouette, obtaining an aerodynamic porosity equal to
 209 0.3, which approximates the porosity of a real tree (Manickathan et al. 2018)
 210 and is consistent with the value of the optical porosity computed with image
 211 processing. The drag coefficient was estimated as $2F/\rho_a U_{ref}^2 A_c$, where F is
 212 the drag force measured by means of a load cell, ρ_a the air density (around
 213 1.18kg/m^3 at 25°), U_{ref} the velocity of the approaching wind measured using
 214 the Pitot tube, and A_c the projected frontal area of the tree. Increasing U_{ref} ,
 215 the drag coefficient converges to a constant value equal to 0.65, which is in
 216 line with the drag coefficient of a real tree (Manickathan et al. 2018), for
 217 Reynolds numbers based on the tree ($Re_t = U_{ref} H_T / \nu$, where H_T is the
 218 tree height) greater than 10^4 . The model trees were inserted in the reference
 219 canyon, arranged according to three different configurations: no trees inside
 220 the canyon (Zero, Fig. 1b), two parallel rows of seven trees spaced 14 cm apart
 221 (Half, Fig. 1c) and two parallel rows of fourteen trees spaced by 7 cm (Full,
 222 Fig. 1d).

223 3 Measurement techniques

224 We used the Laser Doppler Anemometer (LDA) technique, to measure the
 225 streamwise (u), transversal (v), and vertical (w) components of the velocity
 226 field. As detailed below, we first measured simultaneously u and v inside the
 227 canyon only, then we coupled a mirror to the LDA to measure u and w both
 228 inside the canyon and at the roof level. In a third measuring session, the system
 229 LDA-mirror was coupled with a Flame Ionization Detector (FID) to measure
 230 vertical turbulent mass fluxes, both inside the canyon and at the rooftop. The
 231 concentration field was measured with high spatial resolution by means of the
 232 FID alone (Fellini et al. 2022).

233 3.1 Concentration

234 The scalar concentration was measured using a FID model HFR400, suitable
 235 to measure hydrocarbon concentration time series. The instrument is equipped
 236 with a sampling capillary tube 0.3 m long, 1.27×10^{-4} m inner radius, and
 237 imposed pressure drop of 33330.6 Pa, guaranteeing a frequency response of
 238 about 800 Hz (Nironi et al. 2015). The FID works in the range 0-10 V, and
 239 it detects concentration values in the range 0-5000 ppm, with a precision of
 240 about 1-2 ppm. The relation between the electric potential measured by the
 241 FID and the concentration in ppm is a linear function, whose slope coefficient
 242 is calculated by calibrating the instrument at the beginning and at the end

243 of each measurement session (Marro et al. 2020). A variation of $\pm 3\%$ of the
244 coefficient is accepted, as the instrument is sensitive to ambient conditions.
245 Since the wind tunnel is a recirculating system, the background concentration
246 increases with time. Thus, a linearly interpolated value of the background
247 concentration recorded at the beginning and at the end of each measurement
248 is subtracted from the concentration signals.

249 The scalar field was characterized using a three-dimensional measuring
250 grid, whose details are available in Fellini et al. (2022). In the present work,
251 we extract from that dataset a 2D vertical section in the center of the canyon
252 ($x/H=1$), and a 2D horizontal section at the rooftop ($z/H=1$). The measure-
253 ments were performed setting a constant sampling frequency of 1000 Hz and
254 an acquisition time of 120 s. Analysing concentration signals, we verified that
255 the acquisition time is enough long to guarantee a good convergence of the
256 mean and standard deviation of the concentration. To collect more samples
257 for the investigation of the probability density function of the concentration,
258 we extended the acquisition time to 300 s for a limited number of sampling
259 points located along a longitudinal profile in the center of the canyon (x and z
260 coordinates were fixed at $x/H=1$ and $z/H=0.4$, respectively). In the vegetated
261 canyon configurations, a higher number of sampling points were measured, to
262 capture the heterogeneity of the mean concentration profiles.

263 3.2 Velocity

264 The velocity field was measured using a LDA Argon class IV, equipped with
265 a 5 W power laser, emitting two blue and two green beams with wavelengths
266 $\lambda_{blue}=488$ nm and $\lambda_{green}=514.5$ nm, respectively. The beams have a diameter
267 of 0.1 mm and the LDA focal length is 400 mm. The point of intersection of
268 the four beams determines the measuring volume. In dual-beam configuration,
269 the LDA provides the module and the direction of two velocity components
270 simultaneously, notably u and v . To measure the u component together with
271 w , the LDA is coupled with a mirror, which deflects the laser beams (as shown
272 in Fig. 1e). We maintained a data rate of around 1500 Hz, and a sampling time
273 sufficiently long to collect at least 250 000 samples in each measuring point,
274 to obtain a good convergence of the statistical moments of the velocity signal.
275 During the acquisition, the power of the blue and the green beams was set
276 at 800 mW. The seeding of the flow was generated with the fluid SAFEX®-
277 Inside-Nebelfluid "Dräger Spezial W", emitting droplets with dimensions in
278 the range 0.5-2 μm .

279 3.3 Turbulent mass flux

280 The turbulent vertical mass fluxes are evaluated as the cross-correlation be-
281 tween concentration fluctuations and velocity fluctuations, $c'(t)$ and $w'(t)$,
282 respectively. Instantaneous fluctuations are defined as $c'(t) = c(t) - \bar{c}$ and

283 $w'(t) = w(t) - \bar{w}$ respectively, where $c(t)$ is the concentration time series with
 284 the background concentration removed (see section 3.1), $w(t)$ is the vertical
 285 velocity time series, \bar{c} and \bar{w} are their mean, and t is the time. The estimate
 286 of cross-correlation requires concentration and velocity to be measured simul-
 287 taneously, in the same control volume. This can be achieved by coupling the
 288 FID and the LDA (Fig. 1e).

289 The installation of the LDA-FID system and the evaluation of the cross-
 290 correlation were performed following the approaches and methods provided
 291 by Marro et al. (2020). The distance between the measuring volume of the
 292 LDA and the sampling tube of the FID was set at 4 mm, as it is the optimal
 293 distance to avoid flow disturbances caused by the FID and to guarantee that
 294 concentration and velocity measurements refer to the same fluid elements. In
 295 this setup, the time delay between the two signals (Δt_{lag}), due to the travel
 296 of the particles across the sampling tube (see subsection 3.1), was estimated
 297 to be 0.016 s (Marro et al. 2020). The cross-correlation between velocity and
 298 concentration fluctuations ($\overline{w'c'}$) was computed using the sample-and-hold re-
 299 construction and resampling (S+H) method (Kukačka et al. 2012; Marucci
 300 and Carpentieri 2019). Notably, the concentration signal was shifted by Δt_{lag} ,
 301 and resampled on the irregular sampling frequency of $w(t)$, using the nearest
 302 neighbor interpolation since the correspondence between velocity and concen-
 303 tration data was missing. This method is reliable in this application, as it
 304 provides results with less than 6% difference from those of the well-established
 305 slot correlation method (Marro et al. 2020).

306 Flow velocity and turbulent mass fluxes were measured on a 2D vertical
 307 grid along the longitudinal axis of the canyon (the streamwise coordinate is
 308 fixed at $x/H=1$) and on a horizontal grid at the rooftop (fixing the vertical
 309 coordinate at $z/H=0.98$). The vertical grid, being located in the centre of
 310 the canyon, is easily accessible to the experimental equipment (in particular
 311 the system LDA-FID coupled with the mirror) in both the empty and vege-
 312 tated canyons, the horizontal grid, fixed 2 mm below the canyon rooftop, is
 313 used to investigate the flow field and mass transfer between the inner canyon
 314 and the external atmosphere. The vertical grid at $x/H=1$ is composed of five
 315 longitudinal profiles sampled at heights $z/H=[0.2, 0.4, 0.6, 0.8, 0.98]$, whilst
 316 the horizontal section at the rooftop includes three longitudinal profiles at
 317 $x/H=[0.5, 1, 1.5]$. Both sections extend from $y/H=-3.5$ to $y/H=+3.5$. The
 318 longitudinal spacing of the sampling points is 50 mm in the Zero configura-
 319 tion, while it is irregular in the vegetated canyon configurations, due to the
 320 encumbrance of trees, and due to the fact that the mean scalar field is not
 321 homogeneous, so more points were acquired in correspondence of the mean
 322 concentration peaks (Fellini et al. 2022).

323 4 Results

324 In this section, we investigate the influence of tree density on the flow velocity
 325 (Fig. 4-6), concentration statistics (Fig. 7-11), and mass fluxes (Fig. 12-15).

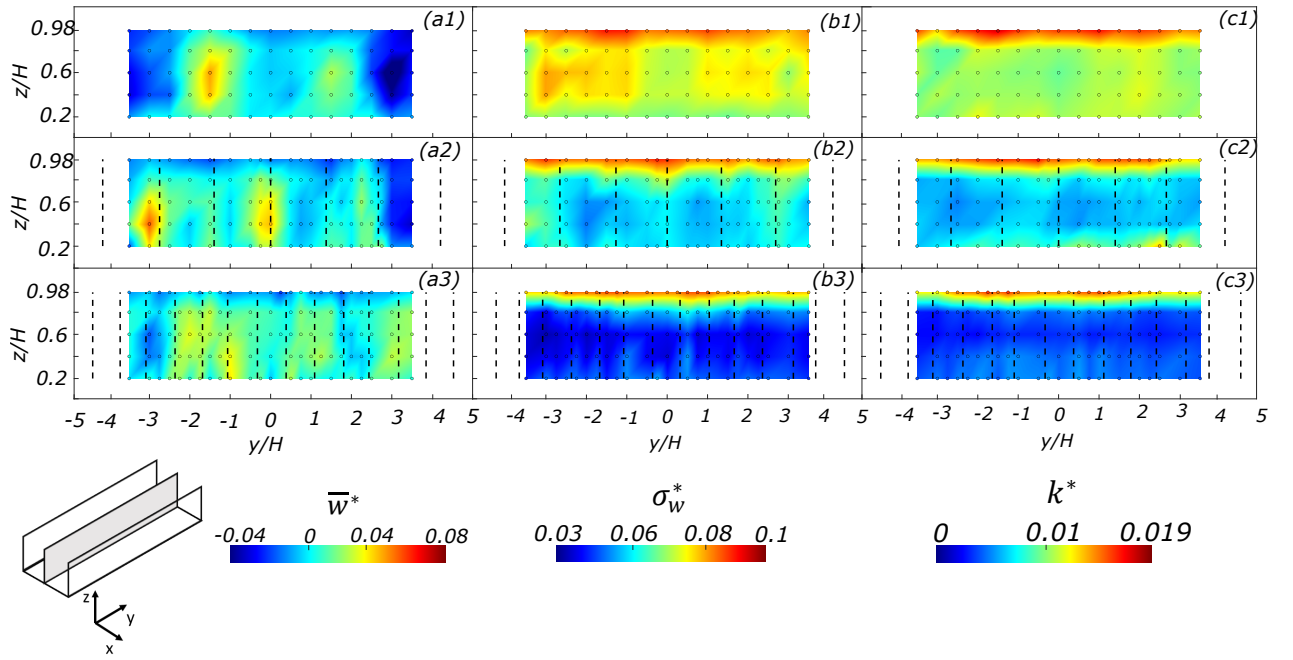


Fig. 4 Two-dimensional sections of mean vertical velocity (a1-a3), vertical velocity standard deviation, (b1-b3) and turbulent kinetic energy (c1-c3), on the plane at $x/H=1$. The Zero (a1, b1, c1), Half (a2, b2, c2), and Full (a3, b3, c3) configurations are shown. Black dashed lines indicate the position of the trees. Colored circles represent the measuring points. The shaded area in the sketch shows the position of the cross-section in the canyon.

326 The mean and the turbulent components of all quantities are shown on vertical
 327 and horizontal sections (located at $x/H=1$ and $z/H=0.98$ or $z/H=1$, respec-
 328 tively), both obtained from linear interpolation of measured data. Moreover,
 329 using instantaneous concentration, velocity, and mass fluxes data we evaluate
 330 the concentration probability density function inside the canyon (Fig. 11) and
 331 the spectra of vertical velocity fluctuations and turbulent mass fluxes at the
 332 rooftop (Fig. 6, 15).

333 4.1 Flow field

334 As we are interested in analyzing the vertical mass transport in the street
 335 canyon, we focus here on the spatial distribution of the mean and standard de-
 336 viation of the vertical velocity, normalized as $(\bar{w}^*, \sigma_w^*) = (\bar{w}, \sigma_w)/U_\infty$, respec-
 337 tively. Positive \bar{w}^* refers to upward flow and negative \bar{w}^* refers to downward
 338 flow. As we mentioned in section 3, we measured also u and v components.

339 Figure 4a1-a3 show the mean vertical velocity in the center of the canyon.
 340 In the Zero configuration (panel a1), the \bar{w}^* field is organized in two sym-
 341 metric zones of upward flow (around $y/H=-1.5$ and $y/H=+1.5$), and three

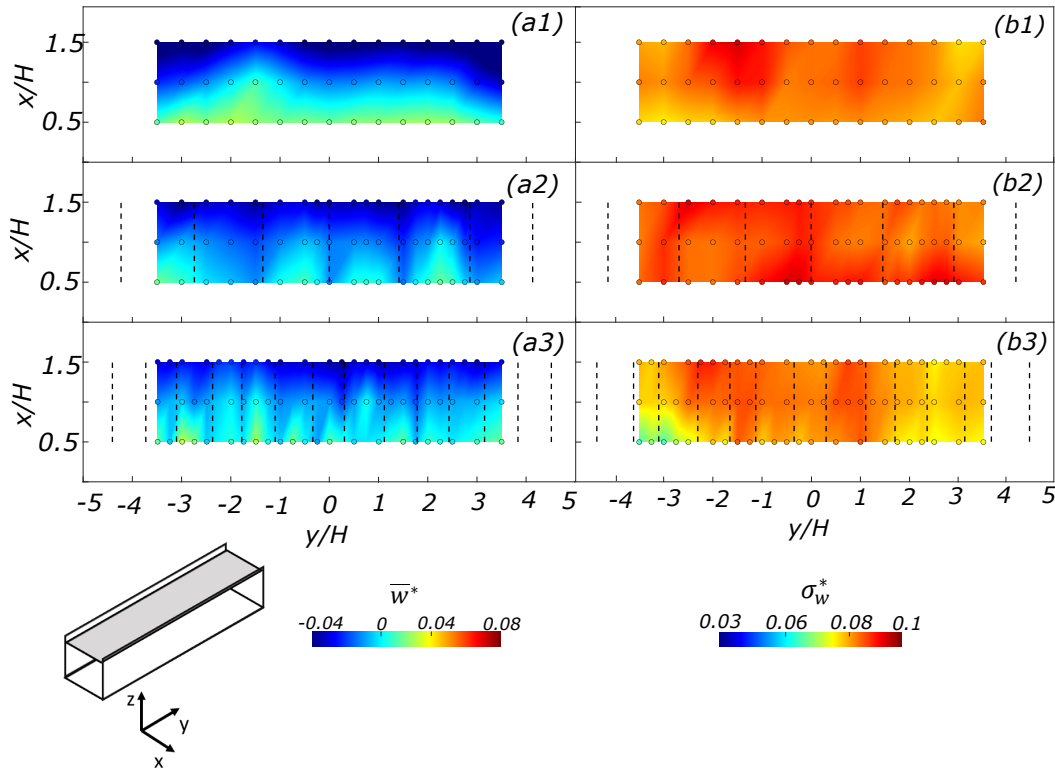


Fig. 5 Two-dimensional sections of mean vertical velocity (a1-a3) and vertical velocity standard deviation (b1-b3), on the plane at $z/H=0.98$. The Zero (a1, b1), Half (a2, b2), and Full (a3, b3) configurations are shown. Black dashed lines indicate the position of the trees. Colored circles represent the measuring points. The shaded area in the sketch shows the position of the cross-section in the canyon.

342 zones of downward flow located at the edges and in the center of the canyon.
 343 The asymmetries in the upward flow regions, are due to tiny uncertainties in
 344 the arrangement of the building-like blocks (Garbero et al. 2010) and slight
 345 inclination of the external flow with respect to the wind tunnel axis (Nironi
 346 et al. 2015). In the Half configuration (panel a2) the succession of positive
 347 and negative zones is still present, but the spatial organization is different: we
 348 identify three zones of positive \bar{w}^* and two zones of negative \bar{w}^* . In the Full
 349 configuration (panel a3), positive \bar{w}^* values prevail and the spatial pattern is
 350 more homogeneous. The mean flow within a urban canyon perpendicular to
 351 the external wind flow is governed by a recirculating cell (Gromke and Ruck
 352 2007; Fellini et al. 2022) as the external flow enters the canyon at the down-
 353 wind wall and exit at the upwind wall. As a consequence, moving toward the
 354 downwind wall of the street canyon, we expect a downward flow to occur and
 355 the presence of trees to lead to a more heterogeneous pattern. Moreover, due
 356 to the recirculation we do not observe a decrease in the mean vertical velocity

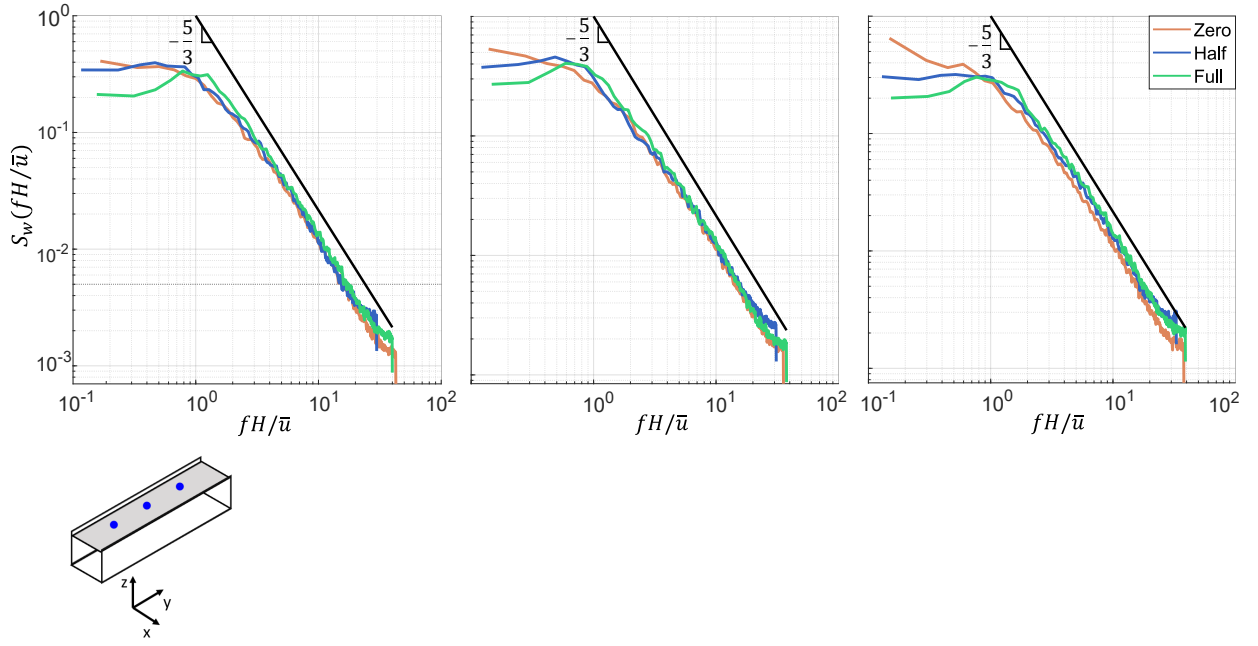


Fig. 6 Spectra of $w'(t)$ calculated in three different sampling points along the central line ($x/H=1$) at the rooftop ($z/H=0.98$): (a) $y/H=-1.5$, (b) $y/H=0$, (c) $y/H=2$. The blue points on the shaded plane in the bottom inset represent the positions where the spectra were calculated.

357 moving towards the ground level. The random shape, size, and orientation of
 358 the model trees produce further asymmetries, even if they are smaller than
 359 the different longitudinal patterns induced by the different tree spacing.

360 Conversely, vegetation does not induce peculiar spatial patterns in the
 361 vertical velocity standard deviation (Fig. 4b1-b3): σ_w^* remains fairly constant,
 362 both along the y and z axes, until the interface between the canyon and the
 363 external flow ($z/H = 0.98$) where it increases sharply, and it reaches the same
 364 value (about 0.08) in all configurations. On average, below the tree crowns, σ_w^*
 365 decreases with the increase in tree density: in the Full configuration, the spatial
 366 average of σ_w^* (calculated by weighting the single values by the area associated
 367 to each measurement point) is 40% lower than in the Zero configuration.

368 In panels c1-c3 of Fig. 4, we analyze the turbulent kinetic energy, estimated
 369 as $k^* = 0.5(\sigma_u^2 + \sigma_v^2 + \sigma_w^2)/U_\infty^2$. In the Zero and Full configurations (panels
 370 c1 and c3), k^* is homogeneous in the interval $z/H=[0.2, 0.8]$. In the Half
 371 configuration (panel c2) it is slightly heterogeneous moving along the vertical
 372 direction: higher close to the ground and lower in the interval $z/H=[0.4, 0.8]$.
 373 The enhanced values of k^* observed close to the ground are due to the fact
 374 that the dampening effect is mainly limited in correspondence of the tree
 375 crowns, while the large spacing between trunks allows the k^* to slightly recover
 376 the intensity it has in the empty canyon. As observed for σ_w^* (panels b1-b3),

the presence of trees dampens k^* : on average, we observe a decrease of 60% between Zero and Full configurations. Moving to the rooftop of the canyon (z/H in the interval $[0.8, 0.98]$), we identify a sharp increase of k^* , regardless of the presence of trees. The increase of both k^* and σ_w^* reveals the presence of a shear layer of thickness $z/H \sim 0.2$, where the turbulence of the external flow is entrained in the cavity flow (Salizzoni et al. 2011; Fellini et al. 2020).

An evident imprinting of the trees can be noticed by comparing the mean vertical velocity patterns at the rooftop among the different configurations (Fig. 5a1-a3). In the non-vegetated canyon (panel a1), \bar{w}^* has a quite homogeneous behavior along the y -axis: negative at the downwind wall, and positive at the upwind wall. Indeed the external flow enters the canyon at the downwind wall and leaves it at the upwind wall, following a recirculating flow structure (Gromke and Ruck 2009). In the vegetated canyons, this pattern is maintained, but it is more heterogeneous at the upwind wall, as trees hinder the vertical flow motion: the upward flow occurs between adjacent trees, and its spatial periodicity increases with tree density (panels a2, a3).

On the other hand, the values of σ_w^* at the rooftop (Fig. 5b1-b3) are almost unaffected by the presence of trees. In the Zero and Half configurations (panels b1 and b2), σ_w^* values are almost homogeneous both in the longitudinal and streamwise directions. In the Full configuration (panel b3), some heterogeneities arise: σ_w^* decreases moving towards the edges of the canyon, mostly at the left upwind corner. In all configurations, σ_w^* values are significantly higher than the one inside the canyon.

To investigate the influence of trees on the scales of the turbulent structures involved in the energy motion at the rooftop of the canyon, we analyze the spectra of the vertical velocity signal, calculated with the Welch method. Once resampled the $w(t)$ signal at a constant sampling frequency of 1000 Hz, the Fourier transform was applied to windows of 500 samples (filtered with the Hamming filter), in order to obtain well-resolved spectra without losing information in the low-frequency range. The final spectrum is the mean of the spectra calculated in each window. In Fig. 6, we report the velocity spectra, calculated in three sampling points along the central profile at the rooftop of the canyon: two points in correspondence of the concentration peaks ($y/H = -1.5$ and $y/H = 2$, as will be shown in section 4.2) and one point in the centre ($y/H = 0$). The three different curves represent the velocity spectra (S_w) in the Zero, Half, and Full configurations, expressed as a function of the non-dimensional frequency fH/\bar{u} . To compare spectra in different vegetation configurations, we referred to the velocity signal normalized as $(w(t) - \bar{w})/\sigma_w$, so that the three curves have the same subtended area, equal to 1. Spectra show a decrease in the energy content of the large-scale structures (non-dimensional frequencies in the range 10^{-1} - 10^0) when the canyon is vegetated, that are likely be responsible for the reduced σ_w^* levels induced by high tree density at the canyon rooftop (pointed out in Fig. 5b3). The decrease in energy associated with large scales with tree density can be attributed to the fact that the characteristic length scales of turbulence are significantly influenced by the decreasing tree spacing observed in the Zero, Half, and Full configura-

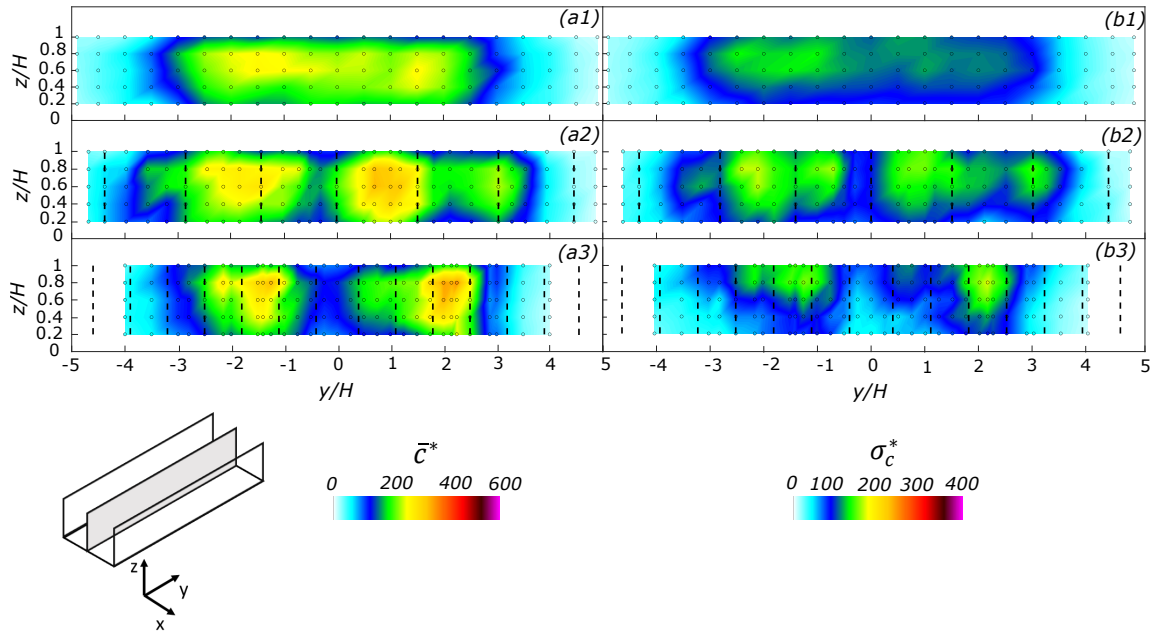


Fig. 7 Two-dimensional sections of mean concentration (a1-a3) and concentration standard deviation (b1-b3), on the plane at $x/H=1$. The Zero (a1, b1), Half (a2, b2), and Full (a3, b3) configurations are shown. Black dashed lines indicate the position of the trees. Colored circles represent the measuring points. The shaded area in the sketch shows the position of the cross-section in the canyon.

423 tions. Conversely, if we look at length scales of the order of magnitude smaller
 424 than the tree spacing (namely, non-dimensional frequencies larger than around
 425 0.7 and 1.4 for the Half and Full configurations, respectively), the three curves
 426 overlap meaning that the effect of the vegetation density is no more detectable.
 427 Indeed, at intermediate scales ($fH/\bar{u} = 10^0-10^1$) the three spectra show an
 428 evident inertial region with constant slope proportional to $-5/3$ (the character-
 429 istic Kolmogorov inertial scaling), regardless of the tree density.

430 4.2 Concentration field

431 As a first step, we recall the main features of the mean concentration field
 432 (investigated in detail by Fellini et al. 2022) and, then, we analyze the concen-
 433 tration standard deviation and the coefficient of variation (Fig. 7-9). We use
 434 the non-dimensional form $(\bar{c}^*, \sigma_c^*) = (\bar{c}, \sigma_c)U_\infty\delta L_s/Q_{et}$, where \bar{c} and σ_c are the
 435 mean and the standard deviation of the concentration time series, respectively,
 436 δ is the height of the boundary layer, L_s is the source length and Q_{et} is the
 437 ethane mass flowrate.

438 Inside the canyon, we notice that, in the range $y/H = [-3, 3]$, the presence
 439 of trees induces a transition from a rather homogeneous mean concentration

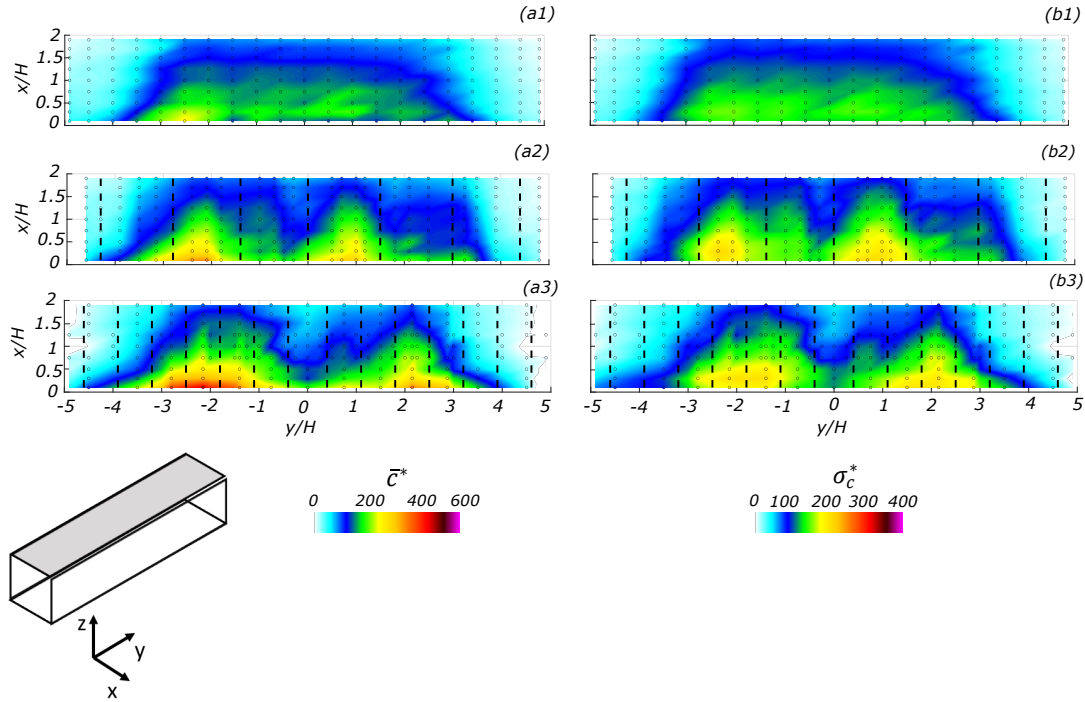


Fig. 8 Two-dimensional sections of mean concentration (a1-a3) and concentration standard deviation (b1-b3), on the plane at $z/H=1$. The Zero (a1, b1), Half (a2, b2), and Full (a3, b3) configurations are shown. Black dashed lines indicate the position of the trees. Colored circles represent the measuring points. The shaded area in the sketch shows the position of the cross-section in the canyon.

440 field to a heterogeneous one (panels a1-a3 of Fig. 7), along the longitudinal
 441 axis. The Half configuration (panel a2) exhibits three zones of higher mean
 442 concentration, whilst the Full configuration (panel a3) is characterized by two
 443 nearly symmetric accumulation zones and a well-defined area of low concen-
 444 tration in the centre of the canyon: here, the concentration is approximately
 445 half the one measured in the accumulation zones. The increase in the spatial
 446 heterogeneity of pollutant concentration with tree density is in contrast with
 447 the behavior of the mean velocity field (shown in Fig. 4a1-a3), which tends
 448 to homogenize with the increase in tree density. Notice that, at the edges, \bar{c}^*
 449 has very low values because the line source does not cover the entire length of
 450 the street canyon. Conversely, the mean concentration does not decrease go-
 451 ing farther away from the ground-level source, as the pollutant is transported
 452 within the canyon by a recirculating structure. For a detailed analysis of the
 453 mean scalar field, see Fellini et al. (2022). The increased variability in the
 454 mean concentration field arises from the complex interaction between larger-
 455 scale motions and the smaller eddies within the canyon, which are generated
 456 by the presence of trees. Given this context, there are reservations about the

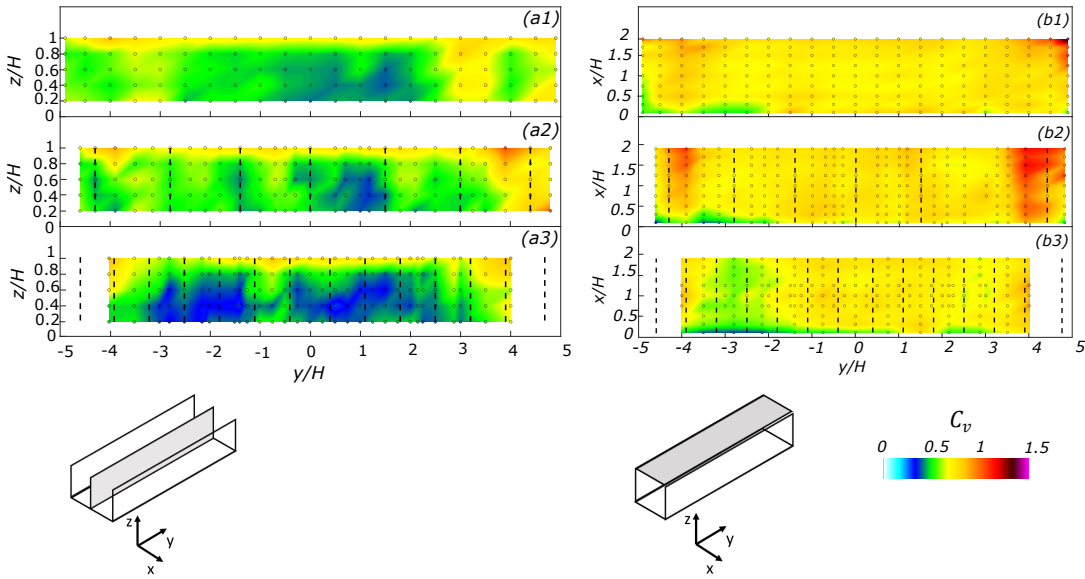


Fig. 9 Two-dimensional sections of the coefficient of variation of the concentration on the plane at $x/H=1$ (left column) and $z/H=0.98$ (right column). The Zero (a1 and b1), Half (a2 and b2), and Full (a3 and b3) configurations are shown. Black dashed lines indicate the position of the trees. Colored circles represent the measuring points. The shaded area in the sketch shows the position of the cross-section in the canyon.

457 suitability of relying on a single parameter, such as the bulk vertical exchange
 458 velocity (u_d), which requires averaging concentrations within the canyon, to
 459 assess the canyon's ventilation potential.

460 The standard deviation of the concentration (Fig. 7b1-b3) follows almost
 461 the same patterns observed for the mean concentration field: a quite homo-
 462 geneous trend in the spatial range $y/H = [-3, 3]$ for the Zero configuration
 463 (panel b1) and concentration fluctuation peaks when trees are added (pan-
 464 els b2 and b3). However, some differences can be pointed out: σ_c^* decreases
 465 slightly along the y -axis in the non-vegetated canyon and shows an increasing
 466 trend in the vertical direction, mostly in the correspondence of peaks in the
 467 Full configuration. Differently from σ_w^* (Fig. 4b1-b3), the average σ_c^* does not
 468 follow a well-defined decreasing trend with vegetation density: with respect
 469 to the Zero configuration, the spatial average of σ_c^* increases of 18% in the
 470 Half configuration and decreases of 6% in the Full configuration. However, the
 471 local maxima of σ_c^* are larger in the presence of trees (see green areas in Fig.
 472 7b2,b3).

473 The mean concentration and the concentration standard deviation patterns
 474 are similar also at the rooftop (Fig. 8). Both show a clear positive gradient
 475 from the downwind wall to the upwind wall, which is almost constant along
 476 the y -axis in the non-vegetated canyon (panels a1 and b1), while it presents
 477 accumulation zones at the upwind wall in the Half and Full configurations

(panels a2, b2, a3 and b3). These high concentration areas enhance the difference in \bar{c}^* and σ_c^* between the two walls: in the Zero configuration, the spatial average of \bar{c}^* at the upwind wall is 58% higher than the one at the downwind wall (note that this is computed by weighting the single value by the spacing between the measurement points along the profiles at $x/H=0.1$ and $x/H=1.9$, respectively), and this difference reaches 66% and 75% in the Half and Full configurations, respectively. For the concentration standard deviation, the difference between the walls is 52%, 57%, and 65% in the Zero, Half, and Full canyons, respectively. As we observed inside the canyon, the presence of vegetation increases the local maxima of σ_c^* (see yellow areas in panels b2 and b3).

In order to highlight differences between mean and standard deviation patterns, in Fig. 9, we investigate the spatial distribution of the coefficient of variation of the concentration, defined as $C_v = \sigma_c/\bar{c}$. As we will see in section 4.2.1, C_v is a key parameter in the analytical models for the probability density function of the scalar concentration in dispersing plumes (Orsi et al. 2021). Inside the canyon (panels a1-a3), the coefficient of variation shows very similar spatial distributions in the Zero and Half configurations, with lower values close to the centre (blue region) and increasing values moving toward the lateral edges of the canyon. Here, the mean and the fluctuating component of the concentration are very low, as there is no scalar emission from the source, thus the evaluation of C_v is affected by large uncertainty. In the Full configuration (panel a3), we observe two regions characterized by weak C_v values, leading to an average decrease of 11% with respect to the Zero configuration. The vegetation-induced transition from a homogeneous field to a heterogeneous one is not as pronounced as for \bar{c}^* and σ_c^* fields, where we observed local differences up to 50% in the Full configuration (see Fig. 7a3,b3), however, the high tree density slightly dampens the concentration fluctuations around the mean, leading to a more heterogeneous pattern with respect to Zero and Half configurations.

At the rooftop (panels b1-b3), C_v is almost homogeneous in all configurations, and 40% larger than within the canyon. However, some heterogeneities appear: higher C_v values at the edges of the canyon and an area of lower C_v around $y/H = -3$ in the Full configurations. Again, the heterogeneities are linked to the uncertainty in the C_v estimate due to the low concentration measured laterally.

4.2.1 Concentration probability density function

The characterization of the probability density function (pdf) of pollutant concentration has several applications including the evaluation of the health risks related to the exposure to high levels of toxic substances, odors assessment, or the estimation of the upcrossing probability. Indeed, these questions require the knowledge of the occurrence probability of instantaneous concentration values above critical thresholds, and, therefore, information about the pdf. Previous studies investigated the pdf of concentration fluctuations arising from

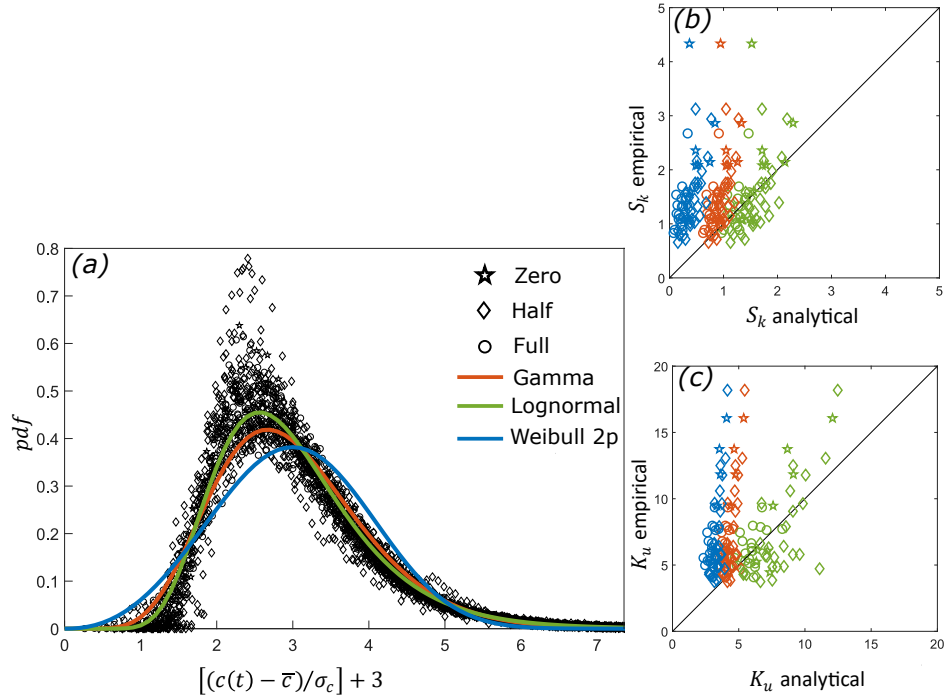


Fig. 10 (a) Empirical pdfs fitted by the gamma (orange), lognormal (green), and Weibull 2p (blue) distributions. The Zero, Half, and Full configurations are considered. (b,c) Scatterplots that compare analytical and empirical skewness and kurtosis.

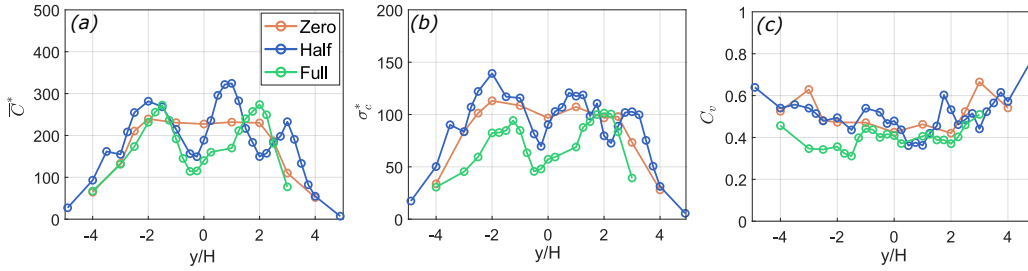


Fig. 11 Longitudinal profile at $x/H=1$ and $z/H=0.4$ of (a) mean concentration, (b) concentration standard deviation, (c) coefficient of variation of the concentration, calculated from the long concentration time series. The Zero (orange), Half (blue), and Full (green) configurations are shown.

522 localised releases in the atmospheric boundary layer (see the review of Cassiani
 523 et al. 2020). Nironi et al. (2015) carried out measurements of concentration
 524 fluctuations inside a plume released by a point source, considering different
 525 source sizes and elevations. They found that the empirical pdf changes shape
 526 with distance from the source, and is well modeled by a gamma distribution.
 527 Other studies report that the lognormal distribution is a suitable model for
 528 plume dispersion in neutral boundary layers (Yassin 2008; Finn et al. 2010),

529 while the two- and three-parameter Weibull distributions provide analytical
 530 formulations to estimate the percentiles of the concentration, who have impor-
 531 tant applications in the odor assessment (Oetl and Ferrero 2017). Conversely,
 532 releases by linear sources were poorly investigated. Li and Bilger (1996) calcu-
 533 lated the statistical moments of the scalar concentration behind a line source
 534 and they found that the empirical pdf is skewed to the right near the source
 535 and it is symmetrical and close to a Gaussian in the far field. Sawford and Sta-
 536 pountzis (1986) compared the pdf calculated from wind-tunnel measurements
 537 of concentration of heat, downstream of a line heating source (performed by
 538 Stapountzis et al. 1986), with a one-dimensional fluctuating model.

539 To fill this gap, we performed a statistical analysis of the pdf of long con-
 540 centration time series, measured along longitudinal profiles in the centre of
 541 the canyon (see Section 3.1). To compare the pdfs calculated in different spa-
 542 tial points and different configurations, we adopt the sample space variable
 543 $\chi(t) = c(t)/\bar{c}$. By means of the method of moments, we fitted the empiri-
 544 cal pdfs with the three analytical distributions mentioned above, that proved
 545 suitable to model the passive scalar concentration pdf in turbulent flows (as
 546 mentioned above): the gamma distribution, the lognormal distribution and the
 547 two-parameters Weibull distribution (Weibull 2p). The analytical pdfs can be
 548 commonly expressed as a function of the unique parameter, C_v :

- 549 1. gamma distribution:

$$P(\chi, \vartheta) = \frac{\vartheta^\vartheta}{\Gamma(\vartheta)} \chi^{\vartheta-1} \exp(-\vartheta\chi) \quad (4)$$

550 where $\Gamma(\cdot)$ is the gamma function and ϑ is the the shape parameter, defined
 551 as $\vartheta = C_v^{-2}$.

- 552 2. lognormal distribution:

$$P(\chi, C_v) = \frac{1}{\chi\sqrt{2\pi\ln(1+C_v^2)}} \exp\left\{-\frac{\left[\ln(\chi) + \ln\left(\frac{1}{\sqrt{1+C_v^2}}\right)\right]^2}{2\ln(1+C_v^2)}\right\} \quad (5)$$

- 553 3. Weibull 2p distribution:

$$P(\chi, C_v) = \frac{C_v^{-1.086}}{a_w} \left(\frac{\chi}{a_w}\right)^{C_v^{-1.086}-1} \exp\left[-\left(\frac{\chi}{a_w}\right)^{C_v^{-1.086}}\right] \quad (6)$$

554 where a_w is the scale parameter, which can be approximated as a function
 555 of C_v (Orsi et al. 2021):

$$a_w = \frac{1}{\Gamma(1+C_v^{1.086})} \quad (7)$$

556 The goodness-of-fit between the empirical and analytical distributions was
 557 evaluated calculating the mean absolute error between the empirical cumula-
 558 tive distribution function (cdf) and the gamma, lognormal, and Weibull 2p
 559 cdfs. Comparing the mean absolute errors (reported in tables 1-3 in the sup-
 560 plementary material), we found that, in all spatial points and in all the tree

561 density configurations, the largest absolute error is associated to the Weibull
 562 2p distribution. This result was expected in the presence of a linear source,
 563 as the Weibull 2p distribution approximates the concentration pdf close to
 564 a point source where the meandering dominates the dispersion process (Orsi
 565 et al. 2021). Conversely, the lowest mean absolute error is associated to the
 566 lognormal distribution in the 80% of the spatial points in the Zero config-
 567 uration, in the 70% in the Half configuration, and in the 100% in the Full
 568 configuration. In the Zero and Half configurations, also the gamma distribu-
 569 tion is a suitable model, indeed it shows a mean absolute error comparable
 570 to the one associated to the lognormal distribution in the 60% of the spatial
 571 points in the Zero configuration and in the 40% in the Half configuration.

572 The empirical pdfs together with the lognormal, gamma, and Weibull 2p
 573 distributions are reported in Fig. 10a. Here, the concentration time series were
 574 normalized as $[(c(t) - \bar{c})/\sigma_c] + 3$, to collapse all the distributions calculated
 575 along the longitudinal profiles into a single distribution with zero mean and
 576 unit variance. As the analytical distributions do not fit negative concentration
 577 fluctuations, the normalized concentration was shifted by a constant equal to
 578 3. The empirical pdfs show a positive skewed bell-shaped behavior in all spatial
 579 points. The same shape is observed in the Zero, Half and Full configurations,
 580 hence it is not affected significantly by vegetation density. A qualitative obser-
 581 vation of the overlap between analytical models and empirical pdfs confirms
 582 that the Weibull 2p distribution is the worst model, while both the gamma
 583 and lognormal distributions reproduce well the empirical pdfs, despite some
 584 discrepancies in the peak and in the left tail. The similarity among the pdfs is
 585 due to the fact that the longitudinal profiles of C_v (which is the only param-
 586 eter that appears in equations 4-6) show variations of the order of 6% (Fig.
 587 11c), so they can be considered homogeneous along y -axis, as the variations
 588 are small compared to the local variations (up to 50%) found in the mean and
 589 turbulent concentration profiles (Fig. 11a,b).

590 We investigated the quality of the fitting also considering the third and
 591 fourth moments. The equations of the analytical skewness (S_k) and kurtosis
 592 (K_u) as a function of C_v are provided in Appendix 1. In panels b and c of
 593 Fig. 10, we report the scatter plots of the analytical versus empirical skewness
 594 and kurtosis, respectively. The skewness is higher than zero, revealing that the
 595 pdfs are skewed to the right. The kurtosis is higher than 3, so the distributions
 596 have fatter tails than the Gaussian distribution. The empirical skewness and
 597 kurtosis are underestimated by the analytical functions provided by both the
 598 Weibull 2p and the gamma distributions. On the other hand, a non-biased
 599 estimation of the empirical moments is obtained from the lognormal distribu-
 600 tion. Indeed, the scatter plot shows a good correlation between the empirical
 601 skewness and kurtosis with the analytical ones, mostly in the Full configura-
 602 tion. We can, therefore, conclude that the lognormal distribution performs a
 603 better fitting of the empirical skewness and kurtosis, and of the entire pdf,
 604 especially with high tree density.

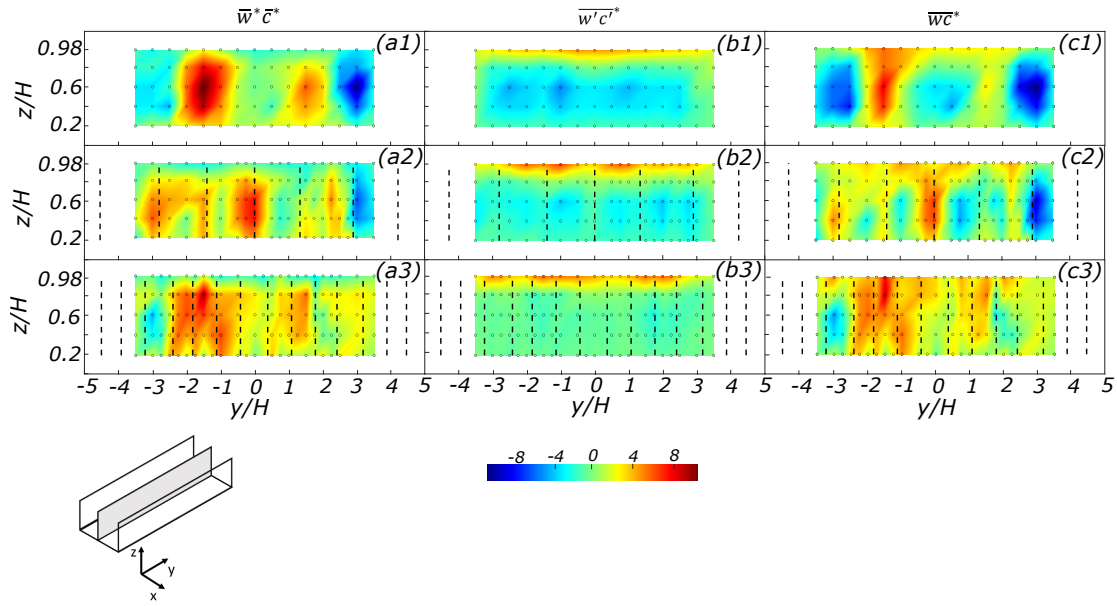


Fig. 12 Two-dimensional sections of convective (a1-a3), turbulent (b1-b3), and total (c1-c3) mass fluxes on the plane at $x/H=1$. The Zero (a1, b1, c1), Half (a2, b2, c2), and Full (a3, b3, c3) configurations are shown. Black dashed lines indicate the position of the trees. Colored circles mark the measuring points. The shaded area in the sketch shows the position of the cross-section in the canyon.

605 4.3 Vertical mass transport

606 We decompose the vertical mass flux ($\overline{w\bar{c}}$) in the mean component ($\overline{w\bar{c}}$) and the
 607 turbulent component ($\overline{w'c'}$) (Fischer et al. 1979). The latter corresponds to the
 608 cross-correlation between velocity and concentration fluctuations measured in
 609 the same control volume (see Section 3.3).

610 Figure 12 shows the non-dimensional mean, turbulent and total mass fluxes
 611 (where vertical velocity and concentration are normalised as defined in the
 612 previous sections), evaluated in the inner canyon. The behavior of the mean
 613 vertical fluxes (Fig. 12a1-a3) is similar to that of the mean vertical velocity
 614 (observed in Fig. 4a1-a3), characterized by a well-organized spatial pattern in
 615 the non-vegetated canyon, that is partially lost increasing the tree density. In
 616 the Zero configuration (panel a1 of Fig. 12), the mean mass flux is positive in
 617 two symmetric regions in the centre of the canyon and negative close to the
 618 edges. The Half configuration (panels a2) is characterized by three zones of
 619 positive mean flux, and three less extended zones of slightly negative flux. In
 620 the Full configuration (panels a3), the mean flux is positive almost in the whole
 621 section, except for an area close to the left edge where it is negative. Turbulent
 622 mass fluxes transport mass down homogeneously in the Zero configuration
 623 (panel b1) and in between the trees in the Half configuration (panel b2),

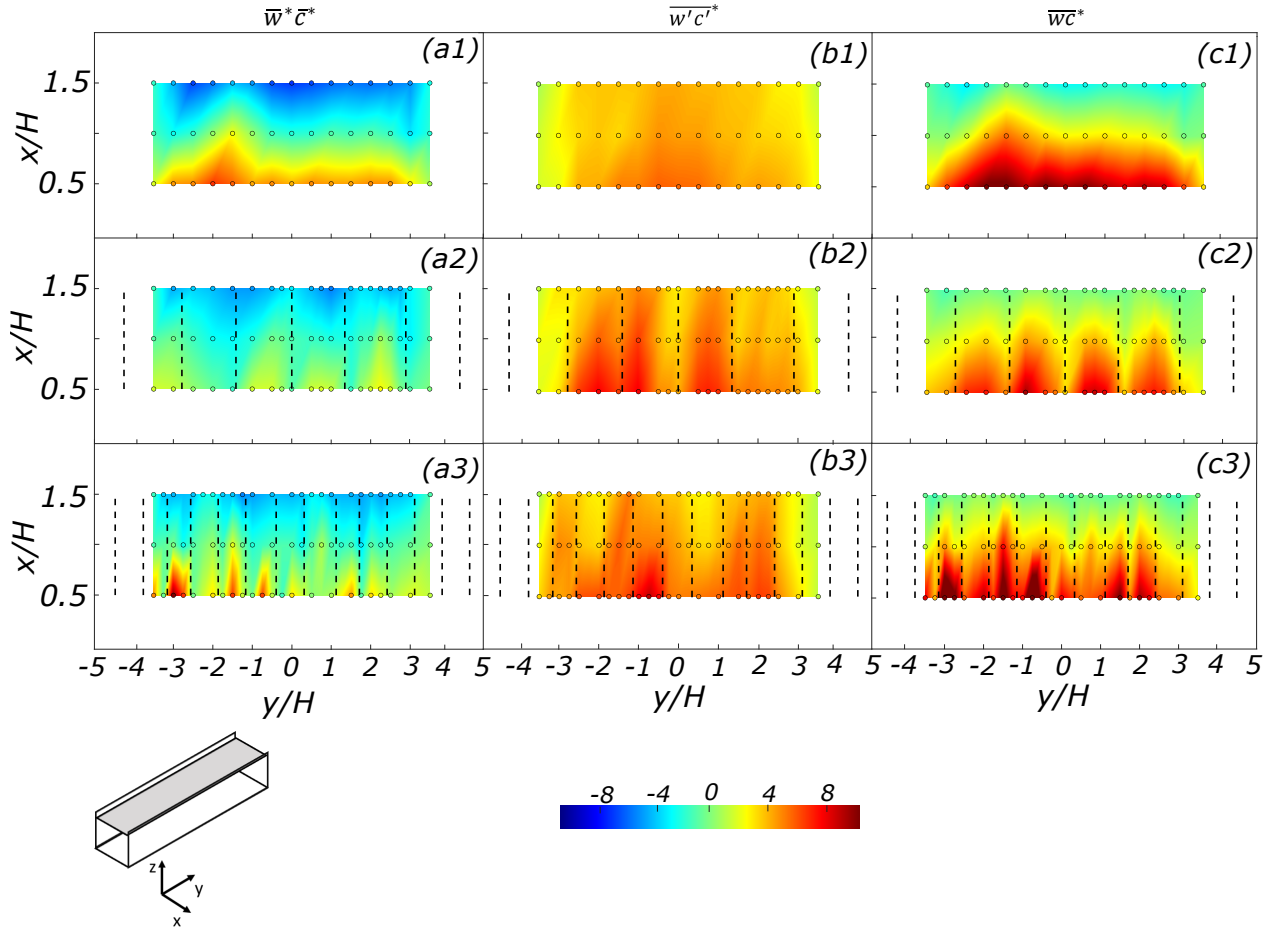


Fig. 13 Two-dimensional sections of convective (a1-a3), turbulent (b1-b3), and total (c1-c3) mass fluxes on the plane at $z/H=0.98$. The Zero (a1, b1, c1), Half (a2, b2, c2), and Full (a3, b3, c3) configurations are shown. Black dashed lines indicate the position of the trees. Colored circles mark the measuring points. The shaded area in the sketch shows the position of the cross-section in the canyon.

624 while they uniformly approach zero in the Full configuration (panel b3). This
 625 reveals that $\overline{w'c'^*}$ is inhibited by an increasing tree density. Regardless of the
 626 presence of trees, $\overline{w'c'^*}$ at the interface between the canyon and the external
 627 flow (notably $z/H=0.98$) sharply increases to the same value (around 8), in
 628 line with σ_w^* and k^* (Fig. 4, panels b1-b3 and c1-c3, respectively). The total
 629 mass fluxes (4c1-c3) have the same spatial distribution of the advective fluxes,
 630 with lower tree density leading to higher heterogeneity along the y -axis. In the
 631 Zero and Half configurations, the contribution of the negative turbulent fluxes
 632 enhances the downward fluxes (blue areas in panels c1 and c2).

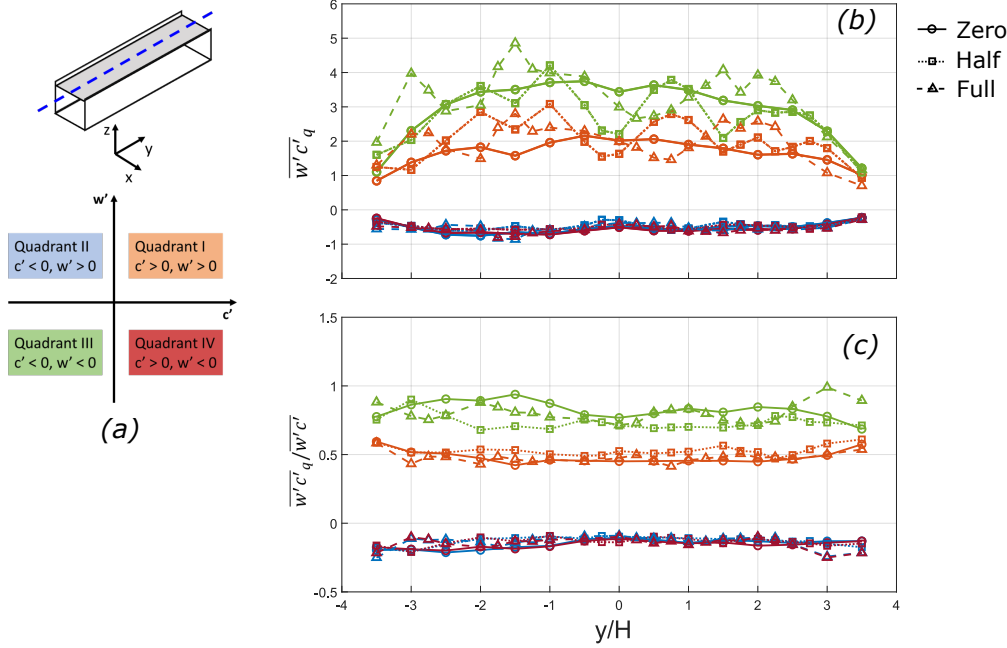


Fig. 14 Quadrant analysis of $\overline{w'c'}$ at the rooftop of the canyon ($x/H = 1$, $z/H = 0.98$). (a) Schematic representation of the quadrants in the plane $\{c', w'\}$. (b) Local quadrant contributions to $w'c'$. (c) Normalized quadrant contributions to $w'c'$. The blue dotted line on the shaded plane in the bottom inset represents the position where the quadrant analysis was performed.

633 The mean mass flux and the mean vertical velocity (Fig. 13a1-a3 and Fig.
 634 5a1-a3, respectively) follow the same behavior at the rooftop as well. In the
 635 non-vegetated canyon (panel a1 of Fig. 13), the mean flux is homogeneous
 636 and negative along the downwind wall ($x/H=1.5$), where the external flow
 637 (without pollutant) enters the canyon, and homogeneous and positive along
 638 the upwind wall ($x/H=0.5$), where the polluted air leaves the canyon. We de-
 639 tect the same streamwise pattern in the vegetated canyons (panels a2, a3), but
 640 the outgoing mean flux is broken into smaller flux segments by the presence
 641 of trees. Moreover, positive $\overline{w^*c^*}$ fluxes are weaker in the Half configura-
 642 tion (panel a2), while their intensity is not homogeneous along y in the Full confi-
 643 guration (panel a3). Turbulent mass fluxes (panels b1-b3) are positive and quite
 644 homogeneous in all configurations with significantly larger values than inside
 645 the canyon (Marucci and Carpentieri 2019), especially in the presence of trees
 646 (panels b2, b3). As already observed inside the canyon, the total vertical mass
 647 fluxes (panels c1-c3) follow the same trend of $\overline{w^*c^*}$, but the strong positive
 648 contribution of the turbulent fluxes enhances the upward transport, and leads
 649 to slightly positive fluxes at the downwind wall. Therefore, the upward total
 650 mass fluxes at the upwind wall are significantly higher than the mean ones,
 651 and they are more heterogeneous with the increase in tree density.

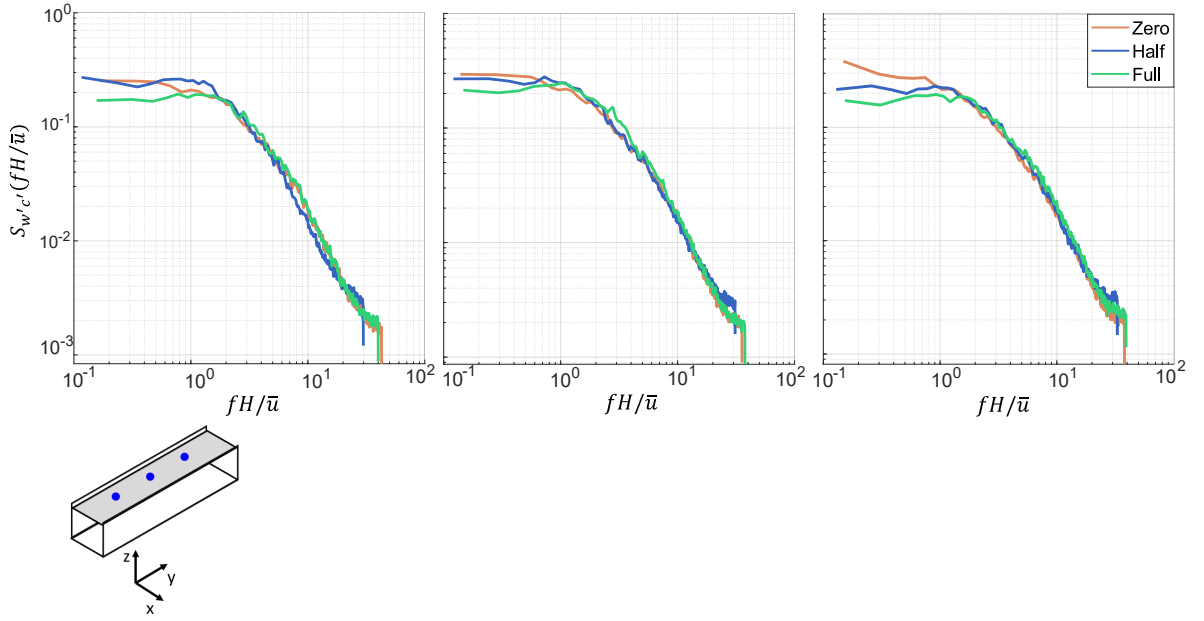


Fig. 15 Spectra of $w'c'(t)$ calculated in three different sampling points along the central line ($x/H=1$) at the rooftop ($z/H=0.98$): (a) $y/H=-1.5$, (b) $y/H=0$, (c) $y/H=2$. The blue points on the shaded plane in the bottom inset represent the positions where the spectra were calculated.

652 In order to understand if the positive turbulent mass fluxes detected at
 653 the rooftop (Fig. 13b1-b3) are due to the entrance of clean external flow or to
 654 the leaving of polluted air from the canyon, we perform the quadrant analysis
 655 (e.g. Di Bernardino et al. 2018). The time series of $w'c'(t)$ are decomposed
 656 on the four quadrants of the Cartesian plane $\{c', w'\}$. In Fig. 14a, we report
 657 a scheme of the quadrant division: quadrant I identifies outflow events with a
 658 concentration higher than the mean, while quadrant III inflow events with a
 659 concentration lower than the mean.

660 In Fig. 14b, we report for a longitudinal profile at the centre of the canyon
 661 rooftop ($x/H = 1$ and $z/H = 0.98$) the local contribution of each quadrant,
 662 defined as the sum of the turbulent fluxes in the quadrant ($\overline{w'c'_q}$, where $q=I, II,$
 663 III, IV). Regardless of the presence of trees, the contributions of quadrants II
 664 and IV, which represent negative turbulent mass fluxes, are negligible relative
 665 to the ones of quadrants I and III, as expected (see Fig. 13b1-b3). The contri-
 666 bution of quadrant III is higher than the one of quadrant I, meaning that the
 667 entrance of external clean air provides an higher contribution to the positive
 668 turbulent mass fluxes in the centre of the canyon rooftop than the exiting of
 669 polluted air. Comparing the different tree density configurations, we notice a
 670 clear distinction between the spatial homogeneity of the profiles of quadrant
 671 I and III in the Zero configuration (continuous lines), and their heterogeneity
 672 in the vegetated canyons (dashed lines). Thus, the presence of trees affects the

673 local contribution of inflow and outflow events. Conversely, the normalized
 674 quadrant contributions to $\overline{w'c'}$ – expressed as the ratio between $\overline{w'c'_q}$ and the
 675 total contribution of all quadrants ($\overline{w'c'}$) – is uniform along the canyon axis,
 676 regardless of the presence of trees (Fig. 14c).

677 We performed the spectral analysis of $w'c'(t)$ signal, to investigate the
 678 turbulent scales involved in the turbulent mass transport at the rooftop of the
 679 canyon. Figure 15 shows the spectra of the normalized mass fluxes ($w'c'(t) -$
 680 $\overline{w'c'}/\sigma_{w'c'}$ (where $\sigma_{w'c'}$ is the standard deviation of $w'c'(t)$ signal), calculated
 681 at $y/H = [-1.5, 0, 2]$, along the central profile at the canyon rooftop. As we
 682 observed in the vertical velocity spectra (Fig. 6), the large-scale structures
 683 dominate the turbulent mass transport in the empty canyon, and the energy
 684 associated to them decreases with the increase in tree density.

685 5 Conclusion

686 The aim of the present study was to investigate the impact of tree-lined avenues
 687 on turbulent flow and concentration fields, and on the vertical mass transport
 688 in an urban street canyon, subject to an external boundary layer. This was
 689 addressed by performing concentration, velocity, and combined concentration-
 690 velocity measurements inside a large canyon ($H/W_c=0.5$) oriented perpendic-
 691 ular to the wind direction, in a wind tunnel. Three different tree densities
 692 were considered: an empty canyon (Zero configuration), a canyon with low
 693 tree density (Half configuration), and a canyon with high tree density (Full
 694 configuration).

695 The increase of vegetation density leads to a partial homogenization of the
 696 mean vertical velocity field and to a reduction of the turbulent kinetic energy,
 697 inside the canyon. However, at the rooftop, the presence of trees does not sig-
 698 nificantly smooth the intensity of velocity fluctuations, but, it partially hinders
 699 the mean vertical velocity at the upwind wall. The tree-induced reduction of
 700 turbulent fluctuations unveils a peculiar effect of high-density vegetation on
 701 turbulent dynamics inside a canyon. This effect deserves the attention of the
 702 scientific community as tree avenues with intersecting crowns are common in
 703 many European cities.

704 Concerning concentration fluctuations, we found that vegetation induces
 705 a transition from an almost homogeneous pattern (characteristic of the non-
 706 vegetated canyon), to a heterogeneous one, both inside the canyon and at the
 707 rooftop. On average, the intensity of concentration fluctuations is not signifi-
 708 cantly smoothed by the presence of trees, rather local maxima are exacerbated
 709 in the vegetated canyons than in the empty one. The coefficient of variation
 710 of the concentration does not show a significant spatial pattern with the tree
 711 density, even if we notice that it slightly decreases in the Full configuration.
 712 Within the canyon, the C_v assumes values that vary between 0.4 and 0.6.

713 The statistical analysis of the concentration time series reveals that the
 714 concentration pdf is skewed towards positive values, it has fatter tails with
 715 respect to the Gaussian distribution, and it maintains the same shape in the

716 different tree density configurations. The gamma and the lognormal distri-
717 butions perform a good fitting of the experimental pdf in the Zero and Half
718 configurations, while in the Full configuration, the lognormal distribution is
719 the best model. In all configurations, the lognormal distribution provides the
720 best estimate of the third and fourth moments.

721 The total mass fluxes are mainly governed by the mean mass fluxes, which
722 in turn show almost the same pattern of the mean vertical velocity. The pattern
723 of mean mass fluxes depends on vegetation: inside the canyon, the mean mass
724 fluxes show a well-organized spatial pattern in the empty canyon, which is lost
725 increasing the tree density and, at the rooftop, the upward mean mass fluxes
726 are hindered by trees. Turbulent mass fluxes are homogeneous and negative
727 inside the non-vegetated canyon, while they are reduced to almost zero with
728 high vegetation density. The vegetation-induced decrease in the turbulent mass
729 fluxes (as well as vertical velocity standard deviation and turbulent kinetic
730 energy) may be responsible for a reduction of the mixing inside the canyon,
731 leading to a more heterogeneous scalar field in the vegetated canyon. At the
732 rooftop, turbulent fluxes are high and positive and their intensity is not affected
733 by the presence of trees. The quadrant analysis reveals that, regardless of the
734 presence of trees, the inflow events of clean air (quadrant III) provides an
735 higher contribution to the positive turbulent mass fluxes at the rooftop than
736 outflow events of polluted air (quadrant I). Moreover, we showed that the
737 normalized contribution of inflow and outflow events to $\overline{w'c'}$ is homogeneous
738 along the longitudinal direction of the canyon. On the contrary, in the presence
739 of trees, the local contribution of outflow (quadrant I) and inflow events is
740 heterogeneous along the longitudinal axis of the rooftop.

741 The spectral analysis of the vertical velocity and turbulent mass fluxes
742 signals revealed that the energy content of large-scale structures decreases
743 with the increase in tree density, or rather the decrease in tree spacing.

744 The wind-tunnel experimental campaign allowed us to highlight the com-
745 plexity of the turbulent mass transport within an urban street canyon, with
746 different vegetation densities. While high vegetation density has been shown
747 to enhance thermal comfort and urban biodiversity, its impact on air quality
748 remains a subject of debate. On one hand tree avenues increase pollutant de-
749 position and regulate local temperature; on the other hand the tree crowns,
750 especially the intersecting ones, hinder the vertical mean flow and dampen
751 turbulent kinetic energy and turbulent mass fluxes. As a consequence of that,
752 at the pedestrian level, the transport and the mixing is less efficient, mostly
753 close to the upwind wall, an issue which has to be considered together with
754 the beneficial effects of high tree density.

755 A limit of the present study was that the experimental equipment employed
756 to measure velocity and mass fluxes (LDA, mirror, LDA-FID system) was not
757 suitable to perform measurements close to the canyon walls, due to the re-
758 flection of the laser beams on the miniatures of trees. This issue prevented us
759 to capture the three-dimensionality of the turbulent flow and scalar transport
760 within the canyon, thus to completely identify the flow dynamics leading to
761 the formation of concentration peaks in a vegetated canyon. However, we pro-

762 vided high-resolution measurements of the mean and turbulent concentration,
763 vertical flow velocity, and mass fluxes in the centre and at the rooftop of the
764 canyon, together with an estimate of aerodynamic porosity and drag coeffi-
765 cient of the model trees. These measurements are useful to validate numerical
766 models, aimed at simulating flow and dispersion in urban-like geometries in
767 presence of vegetation. Moreover, a new experimental campaign is currently
768 underway to investigate the effect of vegetation on the flow field considering
769 different orientations of the canyon with respect to the external flow.

770 Data availability

771 The experimental dataset is available on the website:
772 <https://doi.org/10.5281/zenodo.7757044> (Fellini et al. 2023). We provide con-
773 centration, velocity, and turbulent mass fluxes data within the canyon, and
774 the characterization of the flow field above the buildings.

775 **Acknowledgements** AVDP, LR and PS thank Dept. DIATI (Politecnico di Torino) for
776 having co-funded the PhD scholarship of AVDP in the research project dedicated to the
777 urban atmospheric environment. MR would like to thank École Centrale de Lyon for funding
778 a visiting professorship in 2022. We would like to express our gratitude to Horacio Correia
779 for the technical support in performing the wind tunnel experiments and to Lionel Soulhac
780 for his valuable scientific advice and support.

781 References

- 782 Abhijith K, Kumar P, Gallagher J, McNabola A, Baldauf R, Pilla F, Broderick
783 B, Di Sabatino S, Pulvirenti B (2017) Air pollution abatement performances
784 of green infrastructure in open road and built-up street canyon environments
785 – A review. *Atmospheric Environment* 162:71–86
- 786 Allegrini J, Dorer V, Carmeliet J (2013) Wind tunnel measurements of buoyant
787 flows in street canyons. *Building and Environment* 59:315–326
- 788 Armson D, Stringer P, Ennos AR (2013) The effect of street trees and amenity
789 grass on urban surface water runoff in Manchester, UK. *Urban Forestry &*
790 *Urban Greening* 12(3):282–286
- 791 Blackman K, Perret L, Savory E (2015) Effect of upstream flow regime on
792 street canyon flow mean turbulence statistics. *Environmental Fluid Mechan-*
793 *ics* 15(4):823–849
- 794 Blackman K, Perret L, Savory E (2018) Effects of the upstream-flow regime
795 and canyon aspect ratio on non-linear interactions between a street-
796 canyon flow and the overlying boundary layer. *Boundary-Layer Meteorology*
797 169:537–558
- 798 Buccolieri R, Gromke C, Di Sabatino S, Ruck B (2009) Aerodynamic effects
799 of trees on pollutant concentration in street canyons. *Science of the Total*
800 *Environment* 407(19):5247–5256

- 801 Cassiani M, Bertagni MB, Marro M, Salizzoni P (2020) Concentration fluctu-
802 ations from localized atmospheric releases. *Boundary-Layer Meteorology*
803 177:461–510
- 804 Di Bernardino A, Monti P, Leuzzi G, Querzoli G (2015) Water-channel study
805 of flow and turbulence past a two-dimensional array of obstacles. *Boundary-*
806 *Layer Meteorology* 155(1):73–85
- 807 Di Bernardino A, Monti P, Leuzzi G, Querzoli G (2018) Pollutant fluxes in
808 two-dimensional street canyons. *Urban climate* 24:80–93
- 809 Diener A, Mudu P (2021) How can vegetation protect us from air pollution?
810 A critical review on green spaces’ mitigation abilities for air-borne particles
811 from a public health perspective – with implications for urban planning.
812 *Science of the Total Environment* 796:148,605
- 813 Fellini S, Ridolfi L, Salizzoni P (2020) Street canyon ventilation: Combined
814 effect of cross-section geometry and wall heating. *Quarterly Journal of the*
815 *Royal Meteorological Society* 146(730):2347–2367
- 816 Fellini S, Marro M, Del Ponte AV, Barulli M, Soulhac L, Ridolfi L, Salizzoni P
817 (2022) High resolution wind-tunnel investigation about the effect of street
818 trees on pollutant concentration and street canyon ventilation. *Building and*
819 *Environment* 226:109,763
- 820 Fellini S, Del Ponte AV, Marro M, Salizzoni P (2023) Wind tunnel measure-
821 ments of concentration and velocity in urban geometries with trees. DOI
822 10.5281/zenodo.7757044
- 823 Ferrini F, Fini A (2011) Sustainable management techniques for trees in the
824 urban areas. *Journal of Biodiversity and ecological sciences* 1(1):1–20
- 825 Ferrini F, Fini A, Mori J, Gori A (2020) Role of vegetation as a mitigating
826 factor in the urban context. *Sustainability* 12(10):4247
- 827 Finn D, Clawson KL, Carter RG, Rich JD, Biltoft C, Leach M (2010) Analy-
828 sis of urban atmosphere plume concentration fluctuations. *Boundary-layer*
829 *meteorology* 136:431–456
- 830 Finnigan J (2000) Turbulence in plant canopies. *Annual review of fluid me-*
831 *chanics* 32(1):519–571
- 832 Fischer HB, List JE, Koh CR, Imberger J, Brooks NH (1979) *Mixing in inland*
833 *and coastal waters*. Accademic Press
- 834 Garbero V, Salizzoni P, Soulhac L (2010) Experimental study of pollutant
835 dispersion within a network of streets. *Boundary-layer meteorology* 136:457–
836 487
- 837 Grilo F, Pinho P, Aleixo C, Catita C, Silva P, Lopes N, Freitas C, Santos-
838 Reis M, McPhearson T, Branquinho C (2020) Using green to cool the grey:
839 Modelling the cooling effect of green spaces with a high spatial resolution.
840 *Science of the Total Environment* 724:138,182
- 841 Gromke C, Ruck B (2007) Influence of trees on the dispersion of pollutants in
842 an urban street canyon – experimental investigation of the flow and concen-
843 tration field. *Atmospheric Environment* 41(16):3287–3302
- 844 Gromke C, Ruck B (2009) On the impact of trees on dispersion processes of
845 traffic emissions in street canyons. *Boundary-Layer Meteorology* 131(1):19–
846 34

- 847 Gromke C, Ruck B (2012) Pollutant concentrations in street canyons of differ-
848 ent aspect ratio with avenues of trees for various wind directions. *Boundary-*
849 *Layer Meteorology* 144(1):41–64
- 850 Gromke C, Buccolieri R, Di Sabatino S, Ruck B (2008) Dispersion study in a
851 street canyon with tree planting by means of wind tunnel and numerical in-
852 vestigations – evaluation of CFD data with experimental data. *Atmospheric*
853 *Environment* 42(37):8640 – 8650
- 854 Grylls T, van Reeuwijk M (2021) Tree model with drag, transpiration, shading
855 and deposition: Identification of cooling regimes and large-eddy simulation.
856 *Agricultural and Forest Meteorology* 298:108,288
- 857 Grylls T, van Reeuwijk M (2022) How trees affect urban air quality: It depends
858 on the source. *Atmospheric Environment* 290:119,275
- 859 Hewitt CN, Ashworth K, MacKenzie AR (2020) Using green infrastructure to
860 improve urban air quality (GI4AQ). *Ambio* 49:62–73
- 861 Jaroslowski T, Savory E, Perret L (2020) Roof-level large-and small-scale co-
862 herent structures in a street canyon flow. *Environmental Fluid Mechanics*
863 20:739–763
- 864 Kaimal JC, Wyngaard J, Izumi Y, Coté O (1972) Spectral characteristics
865 of surface-layer turbulence. *Quarterly Journal of the Royal Meteorological*
866 *Society* 98(417):563–589
- 867 Kukačka L, Nosek Š, Kellnerová R, Jurčáková K, Jaňour Z (2012) Wind tun-
868 nel measurement of turbulent and advective scalar fluxes: a case study on
869 intersection ventilation. *The Scientific World Journal* 2012:1–13
- 870 Li J, Bilger R (1996) The diffusion of conserved and reactive scalars behind line
871 sources in homogeneous turbulence. *Journal of Fluid Mechanics* 318:339–372
- 872 Manickathan L, Defraeye T, Allegrini J, Derome D, Carmeliet J (2018) Com-
873 parative study of flow field and drag coefficient of model and small natural
874 trees in a wind tunnel. *Urban Forestry & Urban Greening* 35:230–239
- 875 Marro M, Gamel H, Méjean P, Correia H, Soulhac L, Salizzoni P (2020) High-
876 frequency simultaneous measurements of velocity and concentration within
877 turbulent flows in wind-tunnel experiments. *Experiments in Fluids* 61(12):1–
878 13
- 879 Marucci D, Carpentieri M (2019) Effect of local and upwind stratification
880 on flow and dispersion inside and above a bi-dimensional street canyon.
881 *Building and Environment* 156:74–88
- 882 Merlier L, Jacob J, Sagaut P (2018) Lattice-Boltzmann Large-Eddy Simula-
883 tion of pollutant dispersion in street canyons including tree planting effects.
884 *Atmospheric Environment* 195:89–103
- 885 Moonen P, Gromke C, Dorer V (2013) Performance assessment of large eddy
886 simulation (LES) for modeling dispersion in an urban street canyon with
887 tree planting. *Atmospheric environment* 75:66–76
- 888 Neophytou MA, Markides C, Fokaides P (2014) An experimental study of
889 the flow through and over two-dimensional rectangular roughness elements:
890 Deductions for urban boundary layer parameterizations and exchange pro-
891 cesses. *Physics of Fluids* 26(8):086,603

- 892 Nironi C, Salizzoni P, Marro M, Mejean P, Grosjean N, Soulhac L (2015) Dis-
893 persion of a passive scalar fluctuating plume in a turbulent boundary layer.
894 Part I: Velocity and concentration measurements. *Boundary-layer meteorol-*
895 *ogy* 156(3):415–446
- 896 Nowak DJ, Crane DE (2002) Carbon storage and sequestration by urban trees
897 in the USA. *Environmental pollution* 116(3):381–389
- 898 Oetl D, Ferrero E (2017) A simple model to assess odour hours for regulatory
899 purposes. *Atmospheric environment* 155:162–173
- 900 Oliveira S, Andrade H, Vaz T (2011) The cooling effect of green spaces as
901 a contribution to the mitigation of urban heat: A case study in Lisbon.
902 *Building and environment* 46(11):2186–2194
- 903 Orsi M, Soulhac L, Feraco F, Marro M, Rosenberg D, Marino R, Boffadossi
904 M, Salizzoni P (2021) Scalar mixing in homogeneous isotropic turbulence:
905 A numerical study. *Physical Review Fluids* 6(3):034,502
- 906 Perret L, Basley J, Mathis R, Piquet T (2019) The atmospheric boundary layer
907 over urban-like terrain: influence of the plan density on roughness sublayer
908 dynamics. *Boundary-Layer Meteorology* 170:205–234
- 909 Pietri L, Petroff A, Amielh M, Anselmet F (2009) Turbulence characteristics
910 within sparse and dense canopies. *Environmental fluid mechanics* 9(3):297–
911 320
- 912 Poggi D, Katul G (2007a) Turbulent flows on forested hilly terrain: the re-
913 circulation region. *Quarterly Journal of the Royal Meteorological Society:*
914 *A journal of the atmospheric sciences, applied meteorology and physical*
915 *oceanography* 133(625):1027–1039
- 916 Poggi D, Katul GG (2007b) An experimental investigation of the mean mo-
917 mentum budget inside dense canopies on narrow gentle hilly terrain. *Agric-*
918 *cultural and forest meteorology* 144(1-2):1–13
- 919 Poggi D, Porporato A, Ridolfi L, Albertson J, Katul G (2004) The effect of
920 vegetation density on canopy sub-layer turbulence. *Boundary-Layer Mete-*
921 *orology* 111:565–587
- 922 Poggi D, Katul G, Albertson J (2006) Scalar dispersion within a model canopy:
923 Measurements and three-dimensional lagrangian models. *Advances in Water*
924 *Resources* 29(2):326–335
- 925 Raupach M, Coppin P, Legg B (1986) Experiments on scalar dispersion within
926 a model plant canopy part i: The turbulence structure. *Boundary-Layer*
927 *Meteorology* 35:21–52
- 928 Raupach MR, Antonia RA, Rajagopalan S (1991) Rough-wall turbulent
929 boundary layers. *Applied Mechanics Reviews* 44(1):1–25
- 930 Raupach MR, Finnigan JJ, Brunet Y (1996) Coherent eddies and turbulence
931 in vegetation canopies: the mixing-layer analogy. *Boundary-Layer Mete-*
932 *orology 25th Anniversary Volume, 1970–1995: Invited Reviews and Selected*
933 *Contributions to Recognise Ted Munn’s Contribution as Editor over the*
934 *Past 25 Years* pp 351–382
- 935 Salizzoni P, Soulhac L, Mejean P, Perkins RJ (2008) Influence of a two-scale
936 surface roughness on a neutral turbulent boundary layer. *Boundary-layer*
937 *meteorology* 127(1):97–110

- 938 Salizzoni P, Soulhac L, Mejean P (2009) Street canyon ventilation and atmo-
939 spheric turbulence. *Atmospheric Environment* 43(32):5056–5067
- 940 Salizzoni P, Marro M, Soulhac L, Grosjean N, Perkins RJ (2011) Turbulent
941 transfer between street canyons and the overlying atmospheric boundary
942 layer. *Boundary-layer meteorology* 141(3):393–414
- 943 Sawford B, Stapountzis H (1986) Concentration fluctuations according to fluctu-
944 ating plume models in one and two dimensions. *Boundary-layer meteorol-
945 ogy* 37(1-2):89–105
- 946 Stapountzis H, Sawford B, Hunt J, Britter R (1986) Structure of the temper-
947 ature field downwind of a line source in grid turbulence. *Journal of Fluid
948 Mechanics* 165:401–424
- 949 Van Renterghem T, Forssén J, Attenborough K, Jean P, Defrance J, Hornikx
950 M, Kang J (2015) Using natural means to reduce surface transport noise
951 during propagation outdoors. *Applied Acoustics* 92:86–101
- 952 Yassin M (2008) Probability characteristics of concentration fluctuations in
953 plume dispersal. *Journal of Engineering Sciences* 36(1):115–130
- 954 Zhao Y, Chew LW, Fan Y, Gromke C, Hang J, Yu Y, Ricci A, Zhang Y, Xue
955 Y, Fellini S, et al. (2023) Fluid Tunnel Research for Challenges of Urban
956 Climate. arXiv preprint arXiv:230103001
- 957 Zölch T, Henze L, Keilholz P, Pauleit S (2017) Regulating urban surface runoff
958 through nature-based solutions – an assessment at the micro-scale. *Environ-
959 mental research* 157:135–144

961 **Appendix 1: Expressions of the third and fourth moments of the**
 962 **gamma, lognormal and Weibull distributions**

963 The skewness and kurtosis of the gamma, lognormal and Weibull 2p distribu-
 964 tions are reported as a function of the only parameter C_v :

965 1. gamma distribution:

$$\begin{aligned} S_k(\vartheta) &= \frac{2}{\sqrt{\vartheta}} \\ K_u(\vartheta) &= \frac{6}{\vartheta} + 3 \end{aligned} \quad (8)$$

966 where ϑ is defined as $\vartheta = C_v^{-2}$.

967 2. lognormal distribution:

$$\begin{aligned} S_k(C_v) &= [\exp(\ln(1 + C_v) + 2)] \sqrt{\exp[\ln(1 + C_v^2)] - 1} \\ K_u(C_v) &= \exp[4 \ln(1 + C_v^2)] + 2 \exp[3 \ln(1 + C_v^2)] + 3 \exp[2 \ln(1 + C_v^2)] - 3 \end{aligned} \quad (9)$$

968 3. Weibull 2p distribution:

$$\begin{aligned} S_k(C_v) &= \Gamma\left(1 + \frac{3}{C_v^{-1.086}}\right) C_v^{-3} a_w^3 - 3C_v^{-1} - C_v^{-3} \\ K_u(C_v) &= \Gamma\left(1 + \frac{4}{C_v^{-1.086}}\right) C_v^{-4} a_w^4 - 4S_k C_v^{-1} - 6C_v^{-2} - C_v^{-4}. \end{aligned} \quad (10)$$

969 where

$$a_w = \frac{1}{\Gamma(1 + C_v^{1.086})} \quad (11)$$